

# **SymTC: A Symbiotic Transformer-CNN Net for Instance Segmentation of Lumbar Spine MRI**

*Jiasong Chen<sup>a</sup>, Linchen Qian<sup>a</sup>, Linhai Ma<sup>a</sup>, Timur Urakov<sup>b</sup>, Weiyong Gu<sup>c</sup>, and Liang Liang<sup>a</sup>*

*<sup>a</sup> Department of Computer Science, University of Miami, Coral Gables, FL*

*<sup>b</sup> Department of Neurological Surgery, University of Miami, Coral Gables, FL*

*<sup>c</sup> Department of Mechanical and Aerospace Engineering, University of Miami, Coral Gables, FL*

For correspondence:

Liang Liang, Ph.D.

Department of Computer Science

University of Miami

Ungar Building, Room 330K

Coral Gables, FL, 33146

Tel: (305) 284-8381; Email: [liang@cs.miami.edu](mailto:liang@cs.miami.edu)

## **Abstract**

Intervertebral disc disease, a prevalent ailment, frequently leads to intermittent or persistent low back pain, and diagnosing and assessing of this disease rely on accurate measurement of vertebral bone and intervertebral disc geometries from lumbar MR images. Deep neural network (DNN) models may assist clinicians with more efficient image segmentation of individual instances (disc and vertebrae) of the lumbar spine in an automated way, which is termed as instance image segmentation. In this work, we proposed SymTC, an innovative lumbar spine MR image segmentation model that combines the strengths of Transformer and Convolutional Neural Network (CNN). Specifically, we designed a parallel dual-path architecture to merge CNN layers and Transformer layers, and we integrated a novel position embedding into the self-attention module of Transformer, enhancing the utilization of positional information for more accurate segmentation. To further improve model performance, we introduced a new data augmentation technique to create synthetic yet realistic MR image dataset, named SSMSpine, which is made publicly available. We evaluated our SymTC and the other 15 existing image segmentation models on our private in-house dataset and public SSMSpine dataset, using two metrics, Dice Similarity Coefficient and 95% Hausdorff Distance. The results show that our SymTC has the best performance for segmenting vertebral bones and intervertebral discs in lumbar spine MR images. The SymTC code and SSMSpine dataset are publicly available at <https://github.com/jiasongchen/SymTC>.

**Keywords: Lumbar spine MRI, Medical image instance segmentation, Transformer, Position embedding, Data augmentation**

# 1. Introduction

The intervertebral discs in humans can undergo a profound degenerative process as early in the adolescence [1,2], which can be accompanied by facet arthropathy and hypertrophy. This degeneration can manifest as various conditions, including discogenic low back pain, disc herniation, spinal stenosis, and spondylolisthesis, which may necessitate the implementation of surgical or non-surgical interventions aimed at alleviating pain and restoring normal functionality. Magnetic resonance imaging (MRI) is the most widely used technique for specifically quantifying intervertebral discs degeneration (IDD) by assessing changes in disc geometry deformation and signal strength degradation [3–5]. The information derived from imaging data is of utmost importance for medical professionals in terms of both diagnosing medical conditions and planning appropriate treatments. Furthermore, this information serves as a critical foundation for developing patient-specific computational models, which hold the potential to mature over time and eventually enable accurate predictions of treatment outcomes within clinical settings. Presently, the process of geometry reconstruction, signal measurements, and grading from magnetic resonance (MR) images heavily relies on manual annotation. However, this process is not only time-consuming but also vulnerable to human bias. Consequently, there is an urgent need for automated MR image analysis methods to address these challenges.

In medical imaging, semantic/instance image segmentation, which divides the images into distinct sections at the pixel level so that each pixel belongs to a specific region, has the potential to be carried out through automated techniques [6]. The traditional methods, such as watershed and level set, have demonstrated satisfactory performance in medical image segmentation tasks. The watershed method treats an image as a topological map where intensity represents the altitude of the pixels. The watershed segmentation is determined by the watershed lines on a topographic surface [7,8]. The level set method performs image segmentation by utilizing dynamic variational boundaries [9]. However, the traditional method suffers from the clinical variation of different patients and the noise effect of different medical imaging equipment, resulting in issues such as the over-segmentation [10].

Since the increasingly vast amount of medical imaging data and computational resources have become available, machine learning (ML) methods, especially deep neural network techniques, show superior performance than traditional methods. Convolutional neural network (CNN) has a significant edge over its predecessors in that it possesses the capability to recognize essential components/features without requiring any human intervention [11]. CNNs are specifically designed to effectively utilize spatial and configural information by accepting 2D or 3D images as input. This approach helps to prevent the loss or disruption of structural and configural information in medical images [12]. Various deep CNNs, including UNet++ [13], Attention U-Net [14], MultiResUNet [15] and UNeXt [16] have been proposed for image segmentation for different medical imaging modalities and different organs [e.g., heart [17–19], lung [13], brain [20–23], pancreas [14], gland [23,24], spine [25,26], retina blood vessels [27,28], aorta [29–31], etc]. Although these methods have achieved promising performance, there are still some limitations in a more complex context coping with long-range dependency explicitly due to the intrinsic locality of convolutions.

Recently, Transformer, an ML technique, has shown exceptional performance not only on natural language processing (NLP) challenges like machine translation [32], but also image analysis tasks including image classification [33], image registration[34], image reconstruction[35], and image segmentation[24,36–42]. Various variations of Transformer models have demonstrated that the global information perceived by the self-attention operations is beneficial in medical imaging tasks. TransUNet was the first Transformer-based network specifically for medical image segmentation on the synapse multi-organ segmentation dataset [36]. Wang et al. [24] substituted the original skip connection scheme of U-Net with the proposed UCTransNet that includes a multi-scale Channel Cross fusion Transformer and a Channel-wise Cross-Attention and tested the network on the gland segmentation dataset [43] and synapse multi-organ segmentation dataset [44]. Hatamizadeh et al. [20,21] proposed both UNETR and Swin UNETR for 3D medical imaging segmentation. UNETR utilizes a U-shape network with a vision Transformer as the encoder and a CNN-based decoder. Swin UNETR is constructed by replacing the vision transformer encoder in UNETR architecture with the Swin Transformer encoder. Feng et al. [42] proposed SLT-

Net to utilize CSwin Transformer [46] as the encoder for feature extraction and the multi-scale context Transformer as the skip connection for skin lesion segmentation. Swin-Unet adopted Swin Transformer [37] with shifted windows as encoder and a symmetric Swin Transformer-based decoder with patch expanding layer as decoder for multi-organ segmentation task [17]. Pu et al. [44] proposed a semi-supervised learning framework with Inception-SwinUnet adopting convolution and sliding window attention in different channels for vessel segmentation on small amount of labeled data. Besides the self-attention mechanism, position embeddings are another crucial component of Transformer models. Regarding changing the order of the input, a Transformer model is invariant [32] without position embeddings. However, since text data inherently has a sequential structure, the absence of position information results in the ambiguous or undefined meaning of a sentence [48]. For image segmentation, usually, an image patch is treated as a token, and Transformers process the entire input sequence of tokens in parallel. With position embeddings, a Transformer would be able to differentiate between image patches with similar content that appear in different positions in the input image, which is beneficial for image segmentation applications. A variety of different methods may be used to incorporate the position information into Transformer models. Absolute position encoding and relative position encoding are two main categories to encode a token's position information. Vaswani firstly introduced absolute and relative position embedding in the vanilla Transformer model [32]. Shaw extended the self-attention mechanism with the capacity of effectively incorporating the representation of relative position [49]. Valanarasu et al. [23] proposed a gated position-sensitive axial attention mechanism to cope the difficulty in learning position encoding for the images.

Specifically for lumbar spine research, instance segmentation of MR images is preferred, which not only determines whether or not a pixel belongs to a disc, but also labeling the precise instance to which it belongs [6]. In recent years, most instance segmentation methods for spine image segmentation are based on CNNs-only networks, and only a few Transformer-based networks are employed. For example, Kuang et al. [47] built an unsupervised segmentation network for spine image segmentation using the rule-based region of interest (ROI) detection, a voting mechanism accompanied by a CNN network. Sekuboyina et al. [25] proposed a dual branch fully convolutional network that takes advantages of both low-resolution attention information on two-dimensional sagittal slices and high-resolution segmentation context on three-dimensional patches for effective segmentation of the vertebrae. MLKCA-Unet incorporates multi-scale large-kernel convolution and convolutional block attention into the U-net architecture for efficient feature extraction in spine MRI segmentation [26]. Pang et al. [48] introduced a mixed-supervised segmentation network and it was trained on a strongly supervised dataset with full segmentation labels and a weakly-supervised dataset with only key points. BianqueNet combined new modules with a modified deeplabv3+ network [52], which includes a Swin Transformer-skip connection module, for segmentation of lumbar intervertebral disc degeneration related regions [53].

It was shown that the Transformer-based models only perform effectively when trained on large-scale datasets since the lack of inductive bias [54]. The utilization of Transformer-based networks for medical imaging tasks poses a challenge due to the limited availability of labeled images in medical datasets. Obtaining well-annotated medical imaging datasets presents significantly greater challenges compared to curating traditional computer vision datasets. Dealing with expensive imaging equipment, complex image acquisition pipelines, expert annotation requirements, and privacy concerns are all part of the problematic issues [55]. This scarcity hampers the effective application of Transformer-based models in the medical domain. In such scenarios, the adoption of suitable and feasible data augmentation techniques becomes crucial prior to model training. These techniques can help to increase the effective size of the medical image dataset and improve the performance of the Transformer-based model.

In this study, we propose Symbiotic Transformer-CNN (SymTC) network, an innovative model that effectively combines CNN and Transformers for the automatic lumbar spinal MRI instance segmentation, together with a novel data synthesis method based on statistical shape model (SSM) and biomechanics. For SymTC, a novel relative position embedding (RPE) is proposed for segmentation performance improvement. The SSM-biomechanics-based data synthesis method could generate lumbar spine images with large and plausible deformations, which can be used for model training and evaluation. The code and the generated lumbar spine dataset (SSMSpine) will be publicly available at GitHub when the paper is published.

## 2. Related Work

### 2.1. *Transformer-based Networks for the segmentation of non-spine medical images*

Transformer-based networks have shown promising performance on medical image segmentation because of their ability to capture long-range dependencies. Comparably, the inductive bias of CNN networks benefits from its local connectivity and parameter sharing property. Therefore, many networks, combining CNN and Transformers and leveraging both benefits, have been proposed in the past few years. TransUNet [36] firstly combines CNNs and Transformer in a cascaded manner in its encoder for medical imaging tasks, in which the low-level features are collected from the CNNs and then fed to the Transformer to capture global interactions. Other designs of CNN and Transformer networks, including UNETR [21], UTNet [18], UCTransNet [24], Swin UNETR [20] and MedT [23] have shown better segmentation performances in different medical image modalities, compared to CNN-only networks. UNETR replaces the encoder of a UNet with Transformer layers with 1D learnable positional embedding, and its decoder only has convolution layers [21]. UTNet inserts Transformer layers into a Unet in a sequential manner: a convolution layer followed by a Transformer layer with learnable relative position embedding [18]. UCTransNet embeds Transformer layers into the skip-connections of a Unet with fully learnable absolute position embedding [24]. Swin UNETR replaces the Transformer in UNETR with Swin-Transformer [20]. Medical Transformer (MedT) uses gated-axial Transformer layers in the encoder of a Unet [23]. HSNet used PVTv2 [56] as encoder and a dual-branch structure which Transformer branch and CNN branch fused by element-wise product as decoder for polyp segmentation [57].

### 2.2. *Transformer-based Networks for the segmentation of spine images*

To the best of our knowledge, there are only a few Transformer-based networks [58,59] specifically designed for lumbar spine image segmentation, including EG-Trans3DUNet [58], Spine-transformers [59], APSegmenter [60], and BianqueNet [53]. However, it is worth noting that most of these networks were developed for the segmentation of vertebral bodies using CT modality, which may not be directly applicable to the segmentation of the intervertebral discs in order to study disc degeneration. Among those networks, only the code of BianqueNet is publicly available.

EG-Trans3DUNet combines two vision transformer branches to handle both local patches and resized global spinal CT images [58], and it merges edge characteristics and semantic features generated by a CNN-based edge detection block. Spine-transformers were designed for spinal CT image segmentation with a two-stage pipeline to handle arbitrary Field-Of-View input images [59]. In its first stage, a Transformer with a CNN backbone is utilized as a 3D object detector to locate individual vertebrae, and then the input image is cropped into regions of individual vertebrae. In its second stage, a multi-task encoder-decoder CNN network is applied to each cropped region to segment the vertebra. The source code of the second stage is not publicly available. APSegmenter [60] combines a ViT-style Transformer with a mask Transformer to segment spine X-ray images, and an adaptive postprocessing is applied to further refine the result. BianqueNet [53] employed a resnet101 network to perform feature extraction, followed by upsampling using the Swin Transformer-skip connection module and a double upsampling operations. It also used a multi-scale feature fusion module to generate the segmentation of regions associated with intervertebral disc degeneration.

In addition to the segmentation of vertebral bodies, the segmentation of intervertebral discs (IVDs) is vital for lumbar spinal disease diagnosis and treatment. Since the water content in IVDs cannot be revealed on CT images, currently, MRI is the gold standard imaging modality for the evaluation of IVD pathologies [61]. Our study aims to explore the benefit of combining CNN and Transformer for instance segmentation of lumbar spine MR images.

### 2.3. Self-Attention in Transformer

As opposed to convolutional operations, the self-attention mechanism within a Transformer network has the fundamental advantage of effectively capturing global features and long-range contextual dependency. It uses the Key, Query and Value vectors to better describe the features' connections. Nonetheless, because of the inherited properties of self-attention, it does not retrieve the position information on its own, which is important for instance segmentation. One of the best ways to tackle this problem is to use a well-designed position embedding mechanism to inject the position relationships into the self-attention calculation.

#### 2.3.1. The classic self-attention mechanism with additive position embedding

The plain Transformer is constructed with the multi-head self-attention modules (MHSA), which enable Transformer to capture and utilize more accurate and detailed spatial information [32]. Given an input token set (e.g., image patches)  $X$ , three individual linear transformations ( $W_Q, W_K, W_V$ ) are applied to  $X$  to generate query embedding ( $Q$ ), key embedding ( $K$ ), and value embedding ( $V$ ). Then, the self-attention score,  $Attn$ , is calculated as a scale-product of these three embedding as following:

$$Attn = softmax\left(\frac{QK^T}{\sqrt{d}}\right) \quad (1)$$

$$Out = Attn \times V \quad (2)$$

In the above equations,  $Q = (X + P)W_Q, K = (X + P)W_K, V = (X + P)W_V$ .  $P$  is the encoded position, and  $d$  is the dimension of embedding in each head.  $Out$  is the final output of the self-attention module.

#### 2.3.2. Position Embedding

Without using any position embedding, the self-attention mechanism in Eq.(1) is permutation-invariant and cannot distinguish tokens (e.g., image patches) at different spatial locations. Therefore, it is essential to design efficient position embedding cooperating with the self-attention mechanism.

The attention matrix in the classic self-attention Eq.(1) can be decomposed into three terms:

$$Attn \sim QK^T = \underbrace{XW_Q(XW_K)^T}_{\text{Content-Content}} + \underbrace{P W_Q(XW_K)^T + XW_Q(PW_K)^T}_{\text{Content-Position}} + \underbrace{PW_Q(PW_K)^T}_{\text{Position-Position}} \quad (3)$$

Therefore, the attention considers three interactions among tokens:  $XW_Q(XW_K)^T$  for content to content interaction,  $P W_Q(XW_K)^T + XW_Q(PW_K)^T$  for interaction between content and position, and  $PW_Q(PW_K)^T$  for position to position interaction. As the instance segmentation task is location-specific, a well-designed interaction between content and position could improve self-attention ability to utilize both content and position information to accomplish the instance segmentation task.

Generally, there are mainly two steps to define the position embedding. The first step is defining the position function or distance function, which is used for encoding the position information of input tokens. There are plenty of position functions such as index function, Euclidean distance, and sinusoidal functions etc., The second step is defining methods to incorporate the encoded position information into self-attention.

Absolute position embedding and relative position embedding are two main position representation methods to incorporate the position information into input tokens. Absolute position embedding encodes the

absolute positions of each input tokens as individual encoding vectors, and relative position embedding focuses on the relative positional relationships of pairwise input tokens [62,63]. In the vanilla Transformer designed for NLP [32], it used a combination of absolute and relative position embedding to add position information to the tokens. It is inconclusive whether relative position embedding is better or worse than absolute position embedding, and the answer seems to be dependent on specific applications [48,49,63,64]. Relative position encoding benefits from capturing the details of relative distance/direction and is invariant to tokens' shifting. The intuition is that, in the self-attention mechanism, the pairwise positional relationship (both in terms of direction and distance) between input elements might be more advantageous than absolute position of individual elements [62]. In such a case, position information in Transformer is an extensive research area, and various relative position encodings have been proposed for medical imaging segmentation [54]. For example, UTNet proposed the 2-dimensional relative position encoding by adding relative height and width information [18]. MedT updated self-attention mechanism with position encoding along the width axis with the inspiration of axial attention [23,65,66]. The Parameter-Efficient Transformer added a trainable position vector to the input to encode relative distances [22]. In this work, we propose a novel relative position embedding method for segmentation performance improvement.

### 2.3.3. Self-Attention in the Existing Image Segmentation Models

We compared our model with 15 representative image segmentation models on our dataset, including 11 Transformer-based models and 4 CNN-only models. Our model is significantly different from the others, not only in network structure but also in the self-attention mechanism.

Table 1 summarizes the self-attention mechanisms employed in the existing 11 Transformer-based models. TransUnet and UNETR add the position embedding directly into the input patches [21,36]. Swin-Unet, Swin UNETR, and Inception-SwinUnet incorporate the position embedding into attention score instead of input tokens [17,20,47]. BianqueNet utilized the position embedding within Swin-Transformer [53]. According to the source code, SLT-Net introduces a lepe distance to represent the position bias (embedding), which is directly added into the output matrix [45]. MedT proposed a gated position-sensitive axial attention mechanism where four learnable gates ( $G$ ) control the amount of position embedding contained in key ( $K$ ), query ( $Q$ ) and value ( $V$ ) embeddings [23]. UTNet introduced the 2-dimensional relative position encoding by adding relative position logits along height and width dimensions ( $R_{height}, R_{width}$ ) into the key embedding [18]. HSNet and UCTransNet do not include position embedding in their models [57,24].

**Table 1.** Self-Attention in the existing attention/Transformer-based segmentation models

Model	Self-Attention
Swin UNETR	$\text{softmax} \left( \frac{XW_Q(XW_K)^T}{\sqrt{d}} + R \right) (XW_V)$ <p>Note: <math>R</math> is relative position bias in the reference</p>
SLT-Net	$\text{softmax} \left( \frac{XW_Q(XW_K)^T}{\sqrt{d}} \right) (XW_V) + \text{lepe}(XW_V)$ <p>Note: <math>\text{lepe}</math> is a convolution kernel</p>
UNETR	$\text{softmax} \left( \frac{(X + P)W_Q((X + P)W_K)^T}{\sqrt{d}} \right) (X + P)W_V$
Inception-SwinUnet	$\text{softmax} \left( \frac{XW_Q(XW_K)^T}{\sqrt{d}} + R \right) (XW_V)$ <p>Note: <math>R</math> is relative position bias in the reference</p>

HSNet	$\text{softmax}\left(\frac{XW_Q(XW_K)^T}{\sqrt{d}}\right)(XW_V)$
Swin-UNet	$\text{softmax}\left(\frac{XW_Q(XW_K)^T}{\sqrt{d}} + R\right)(XW_V)$ Note: $R$ is relative position bias in the reference
TransUNet	$\text{softmax}\left(\frac{(X+P)W_Q((X+P)W_K)^T}{\sqrt{d}}\right)(X+P)W_V$
MedT	$\text{softmax}\left(XW_Q(XW_K)^T + G_QXW_Q(R_Q)^T + G_KXW_K(R_K)^T\right)(G_{V_1}XW_V + G_{V_2}R_V)$ Note: $G_Q, G_K, G_{V_1}, G_{V_2}$ are learnable parameters for gating mechanism. $R_Q, R_K, R_V$ are the position bias for Query, Key, and Value
UTNet	$\text{softmax}\left(\frac{XW_Q(XW_K + R_{width} + R_{height})^T}{\sqrt{d}}\right)XW_V$ Note: $R_{width}$ and $R_{height}$ are the relative height and width information
UCTransNet	$\text{softmax}\left(\frac{X_cW_Q(X_cW_K)^T}{\sqrt{d}}\right)(X_cW_V)$ Note: $X_c$ is composed of image channels instead of image patches.
BianqueNet	$\text{softmax}\left(\frac{XW_Q(XW_K)^T}{\sqrt{d}} + R\right)(XW_V)$ Note: $R$ is relative position bias in the reference

### 3. Methods

In this section, we depict the overall architecture of our SymTC network, and explain the pipelines and modules in detail, including TC modules, merge modules, novel self-attention with relative position embedding, and data augmentation. At the end, we provide the loss function for model training.

#### 3.1. The architecture of our SymTC network

The overall architecture of our network is shown in Figure 1, including TC modules (TCM), Merge modules, and a segmentation head. TC modules utilize Transformer and CNN synthetically, which serve as a feature extractor for yielding hierarchies of features. The Merge modules fuse multi-scale feature maps. The segmentation head is used for generating the final instance segmentation masks. The overall diagram of SymTC resembles a U-Net [67], and novelties are in the TC modules that set out network apart from the others.

The network works as follows. First, a 2D sagittal slice of spine MR image  $I \in \mathbb{R}^{1 \times 512 \times 512}$  is processed along the encoder path. From the encoder part, we can obtain three levels of semantic features  $A_i \in \mathbb{R}^{C_i \times \frac{H}{S_i} \times \frac{W}{S_i}}$ , where  $i \in \{1, 2, 3\}$ ,  $C_i \in \{32, 128, 512\}$  and  $S_i \in \{1, 4, 16\}$ . Subsequently, the bottleneck feature is sent to the decoder path for progressively upsampling. The lower-level hierarchical features  $A_1, A_2$ , and  $A_3$  and the

corresponding high-level features  $B_1, B_2$  and  $B_3$  at the decoder side are then fused in the Merge modules for obtaining the pyramid feature  $M_i \in \mathbb{R}^{C_i \times \frac{H}{S_i} \times \frac{W}{S_i}}$ . Thereafter, the final feature  $M_1$  is sent into a refine module (TC module) followed by the segmentation head to obtain the prediction masks  $\hat{Y} \in \mathbb{R}^{12 \times 512 \times 512}$ .

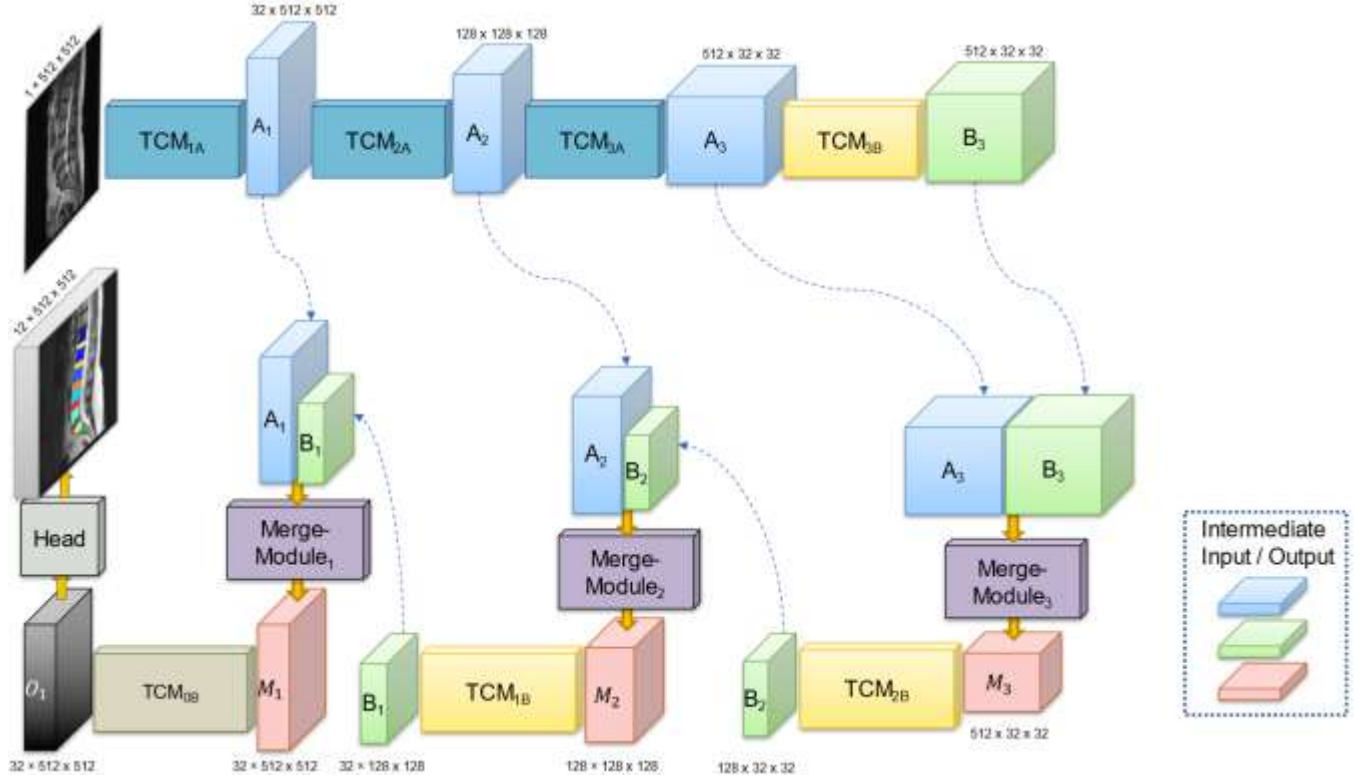


**Fig. 1.** The architecture of SymTC

### 3.2. TC Module with parallel CNN and Transformer paths

Based on the two properties of CNN and Transformer: (1) CNN can model the interaction between adjacent features in the same receptive field via a shifted convolution window. (2) Transformer has the excellent ability for incorporating global features and perceiving long-range dependencies, some networks have been proposed for fusing CNN and Transformer to combine their advantages. Inspired by TransUnet for combining CNN and Transformer in a serial order, we introduce a symbiotic module (TC module) for combining two parallel CNN and Transformer paths. The proposed TC Module integrates the advantages of both CNNs and Transformers to enhance the capability not only to capture more accurate and detailed structural and spatial information, but also to distinguish the boundaries between vertebral bodies and intervertebral discs (IVDs). The architecture of TC module is shown in Figure 2. There are two paths taking the same input in a TC module, including CNN path and Transformer path.

The CNN path in the TC module is a residual block consisting of  $5 \times 5$ ,  $1 \times 1$  and  $3 \times 3$  convolutional filters along with shortcut/skip connections, which is the basic ResNet architecture. The Transformer path in TC module follows the basic architecture of ViT [54]. The input goes to convolutional patch embedding and then is sent to  $N$  layers of Transformer blocks, each block adopts a modified multi-head self-attention layer with relative position embedding (RMHA) for feature extraction and a feed-forward layer. Since we give equal importance to CNN and

Transformer, the two parallel paths work synthetically and mutualistically. Subsequently, feature maps of two paths are concatenated and fed to norm and ReLU layers.

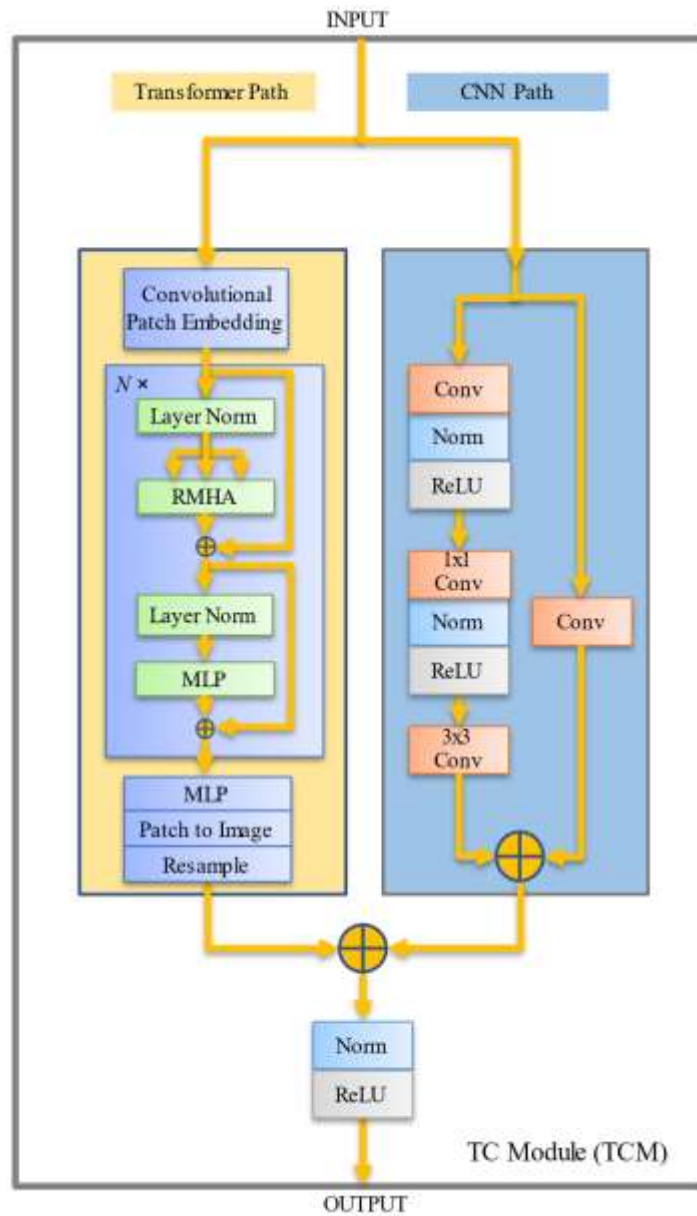


**Fig. 2.** The architecture of TC Module in SymTC, which consists of a CNN path (upper) for local features and a Transformer path (lower) for generating global features. “Norm” refers to GroupNorm or LayerNorm.

Our default configuration of Transformer path in the TC module consists of 2 Transformer layers ( $L=2$ ), an embedding size of 512, and 16 attention heads. We employed three different patch sizes for the TC module:  $16 \times 16$ ,  $4 \times 4$  and  $1 \times 1$ . Specifically, the resolution of  $16 \times 16$  was applied to the first and second TC module, while the resolutions of  $4 \times 4$  and  $1 \times 1$  were utilized in the third and fourth blocks, respectively. This variation in patch sizes allows for capturing different levels of details and context within the input data across different stages of the network.

### 3.3. Novel Self-Attention with Relative Position Embedding in SymTC

We propose a novel relative position embedding to improve segmentation performance. We redefine the attention score matrix by modifying the content-content and content-position components, while eliminating the position-position component, as delineated in Eq.(4):

$$A = \text{softmax} \left( \frac{XW_Q(XW_K)^T R_1 + XW_Q R_2}{\sqrt{d}} \right) \quad (4)$$

In the above Eq.(4),  $R_1$  and  $R_2$  are two matrices encoding relative positions between tokens, which are significantly different from the position encoding methods listed in Table 1.  $X$  is a matrix containing all of the input tokens. The utilization of these relative position components may more effectively include position information. Consequently, the modified attention restructures the content-content and content-position components through the integration of our novel relative position embedding.

To better explain Eq.(4) with more details, we expand it from the perspective of individual tokens. For relative position encoding, we redefine query and key by incorporating the sinusoidal functions to effectively capture the relative position information, which is illustrated by Eq.(5) and Eq.(6).

$$q_i = \begin{bmatrix} x_i W_Q \odot \cos(p_i W_1 + b_1) \\ x_i W_Q \odot \sin(p_i W_1 + b_1) \\ x_i W_Q \odot \cos(p_i W_2 + b_2) \\ x_i W_Q \odot \sin(p_i W_2 + b_2) \end{bmatrix} \quad (5)$$

$$k_j = \begin{bmatrix} x_j W_K \odot \cos(p_j W_1) \\ x_j W_K \odot \sin(p_j W_1) \\ \cos(p_j W_2) \\ \sin(p_j W_2) \end{bmatrix} \quad (6)$$

In the above equations,  $x_i$  and  $x_j$  denote the input token- $i$  and the input token- $j$  (e.g., two image patches) in the format of row vectors.  $p_i$  and  $p_j$  are the absolute position vectors of token- $i$  and token- $j$ .  $W_1$  and  $W_2$  are trainable weight matrices, and  $b_1$  and  $b_2$  are trainable bias vectors, which are used inside the sine and cosine functions to generate different frequency components.  $\odot$  denotes element-wise multiplication between two vectors.

Each entry,  $a_{ij}$ , of the attention score matrix,  $A$ , is proportional to the scalar dot product of the query vector  $q_i$  and the key vector  $k_j$ , which can be derived from the following three equations:

$$q_i \odot k_j = x_i W_Q \odot x_j W_K \odot \cos(p_i W_1 + b_1) \odot \cos(p_j W_1) + x_i W_Q \odot x_j W_K \odot \sin(p_i W_1 + b_1) \odot \sin(p_j W_1) \\ + x_i W_Q \odot \cos(p_i W_2 + b_2) \odot \cos(p_j W_2) + x_i W_Q \odot \sin(p_i W_2 + b_2) \odot \sin(p_j W_2) \quad (7)$$

$$\text{dot}(q_i, k_j) = \text{sum}(q_i \odot k_j) \\ = \text{sum} \left( x_i W_Q \odot x_j W_K \odot \cos \left( (p_i - p_j) W_1 + b_1 \right) + x_i W_Q \odot \cos \left( (p_i - p_j) W_2 + b_2 \right) \right) \quad (8)$$

$$a_{ij} = \frac{\exp[\text{dot}(q_i, k_j)]}{\sum_{j'} \exp[\text{dot}(q_i, k_{j'})]} \quad (9)$$

In the above equations,  $\text{sum}$  computes the summation of all elements. The attention score between the two tokens,  $a_{ij}$ , is a function of the relative position vector  $p_i - p_j$ , which is modulated by cosine functions with

different frequencies and phases. We add bias into the Eq.(5), so that the cosine functions in Eq.(8) may have different phases. The compound relative position encoding, which incorporates both sine and cosine functions in Eq.(5) and Eq.(6), effectively captures the relative position information of the input.

The final output of the attention module contains not only the original term in Eq.(2) but also a new term related to the relative positions. The  $i$ -th row of the final output is given by:

$$out_i = Linear((A_i X W_V)^T) + Linear(\sum_j a_{ij}(p_i - p_j)) \quad (10)$$

In the above Eq.(10),  $A_i$  is the row- $i$  of the attention score matrix  $A$ ,  $Linear$  denotes a linear layer with trainable weight and bias. We note that, in the actual implementation,  $W_Q$  and  $W_K$  are replaced by MLPs.

### 3.4. Novel data augmentation/synthesis method based on SSM and biomechanics

For medical image data augmentation, elastic deformation is often used for nonlinear deformation of the images to increase diversity of training data [67]. Briefly, the input space is discretized by a grid, and a random displacement field on the grid is generated by sampling from a normal distribution with standard deviation equal to  $\sigma \times$  grid resolution (i.e., the size of a grid cell). The parameter  $\sigma$  determines deformation magnitude. To ensure a large deformation with diffeomorphism, the grid needs to be coarser than the input size (i.e.,  $512 \times 512$ ). In this study, we applied two successive elastic deformations to each training image, with grid sizes of  $9 \times 9$  and  $17 \times 17$ . As shown in Figure 3, when the deformation parameter  $\sigma$  is larger than 0.5, the generated images and spine shapes are highly unrealistic. Figure 4 shows two impractical synthesis instances using elastic deformation with  $\sigma$  is 0.5. To avoid unrealistic shapes, we used  $\sigma = 0.25$  in the experiments.

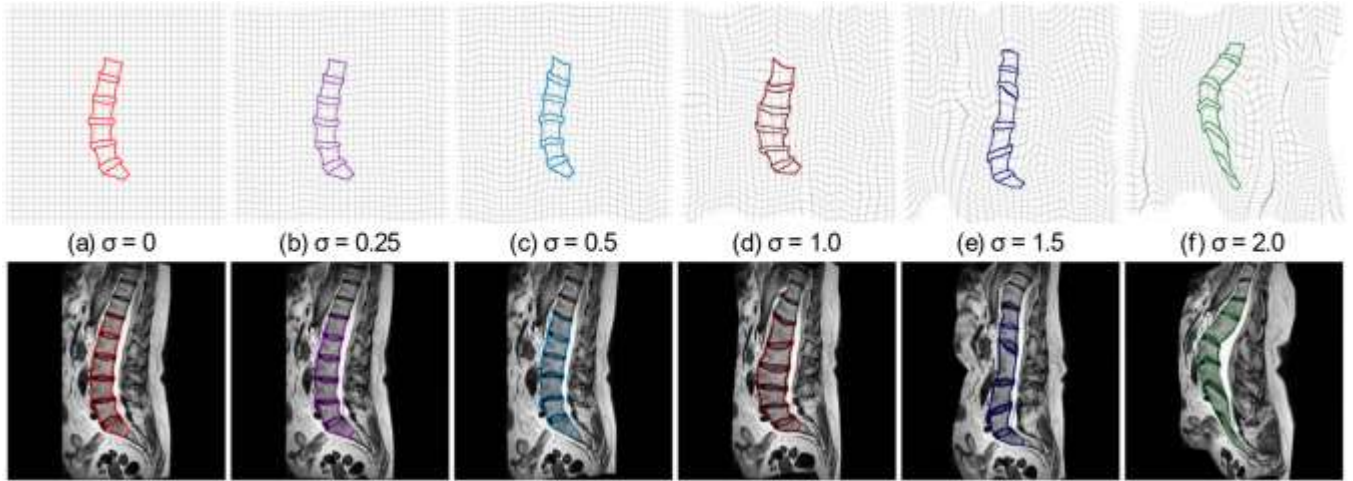


**Fig. 3.** Data augmentation/synthesis examples using elastic deformation with  $\sigma$  from 0 to 2.0.

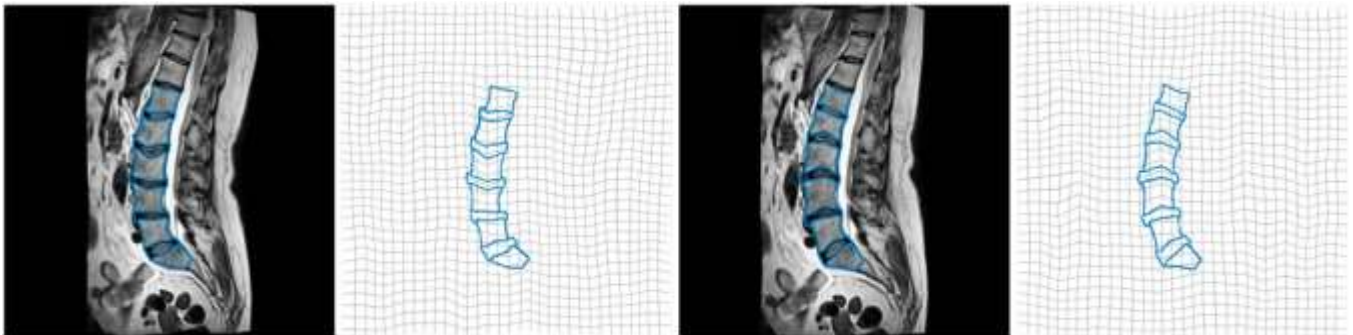


**Fig. 4.** Impractical synthesis instances using elastic deformation with  $\sigma = 0.5$ .

In this work, we developed a new method to synthesize lumbar spine MR images suitable for model training and evaluation. First, we built a statistical shape model (SSM) of lumbar spine shapes (i.e., contours of discs and vertebrae) in a dataset set, and the SSM represents the probability distribution of lumbar spine shapes. We refer the reader to the reference papers [68–72] for the details of constructing an SSM. By sampling from the SSM, different lumbar spine shapes can be generated, and each generated lumbar spine shape could be considered from a virtual patient. We note that the SSM technique has been used to generate virtual but realistic patient geometries in many applications, such as generating aortic aneurysm geometries [73–75]. Given a lumbar spine shape, if a lumbar spine MR image can be generated and consistent with the shape, then we will have a new sample with ground-truth. For this purpose, we developed a biomechanics-based method to generate a lumbar spine MR image  $\tilde{I}$  from a lumbar spine virtual shape  $\tilde{S}$  by using a reference image  $I$  with its ground-truth shape  $S$ . Intuitively speaking, a nonlinear spatial transform from the shape  $S$  to the virtual shape  $\tilde{S}$  is determined by using biomechanics principles [76–78], and then  $\tilde{I}$  is obtained by applying the spatial transform to  $I$ . The generated images are visually plausible, as shown in Figure 5.

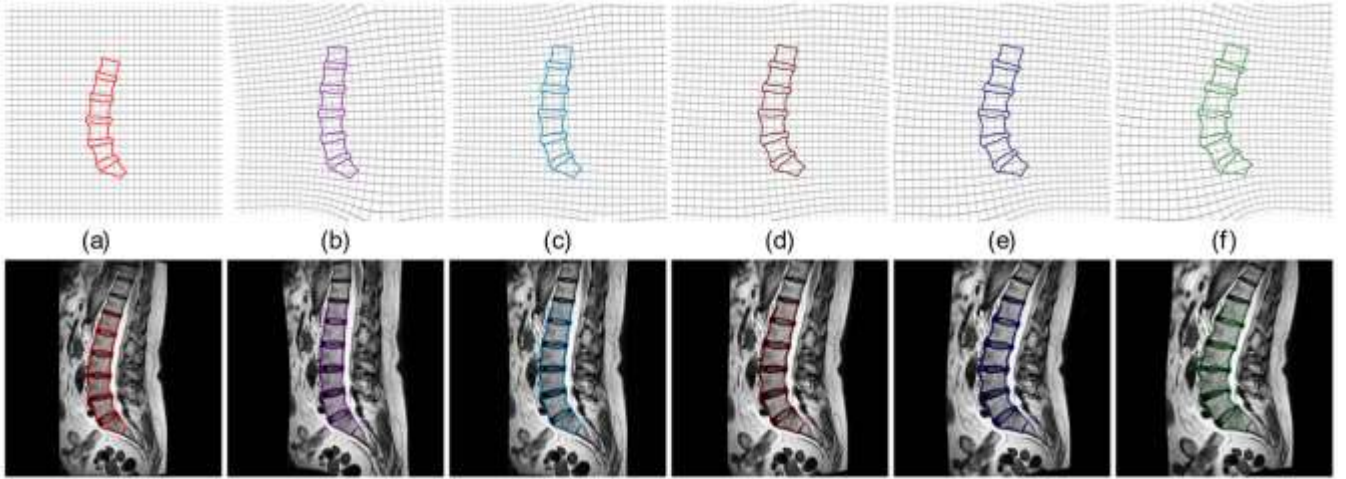


**Fig. 5.** data augmentation/synthesis examples (a-f) using our method. Please zoom in for better visualization.

In the implementation, we obtain the spatial transform  $T$  from  $\tilde{S}$  to  $S$ , and apply the spatial transform  $T$  to a regular mesh grid around the virtual shape  $\tilde{S}$  to obtain a deformed grid in the space of the reference image  $I$ , and then  $\tilde{I}$  is obtained by interpolating pixel values of  $I$  at each node of the deformed grid, i.e.,  $\tilde{I}(x, y) = I(T(x, y))$  where  $(x, y)$  denotes a 2D spatial point and  $T(x, y)$  is the transformed point. By using biomechanics and finite element analysis (FEA), the spatial transform, i.e., the deformation field on the mesh grid, is obtained by minimizing the following energy/loss function  $\Pi$ :

$$\Pi = \int_V \Psi dV + \lambda \cdot \text{avg}_i \|T(\tilde{S}(i)) - S(i)\|^4 \quad (11)$$

In the above Eq.(11),  $V$  represents the undeformed mesh grid of the image  $\tilde{I}$  to be generated,  $\tilde{S}(i)$  is the  $i$ -th point location of the shape  $\tilde{S}$ ,  $T(\tilde{S}(i))$  is the transformed point location that needs to be equal to  $S(i)$ , and  $\|\bullet\|$  denotes vector L2 norm.  $\text{avg}$  is the average operator.  $\lambda$  is a weight constant (set to 16 in experiments).  $\Psi$  is the strain energy density function that is determined by deformation and mechanical property of soft biological tissues around the lumbar spine. From the perspective of FEA and biomechanics, the Eq.(11) simulates the scenario that under the external “force” proportional to  $T(\tilde{S}(i)) - S(i)$  at each point of the lumbar spine shape, the soft biological tissues of human body will deform and reach to an equilibrium state of minimum energy. To speed up the optimization process, we use a deep neural network with sine activation functions to parameterize the transform  $T$ , i.e.,  $T(x, y) = \text{DNN}(x, y)$ , and then the energy function in Eq.(11) becomes a function of the DNN internal parameters. The energy optimization problem is resolved by adjusting/optimizing the parameters of the DNN. Once the optimization is done, the deformation field is obtained and then the image  $\tilde{I}$  is generated. Since our goal is to

generate plausible images for model training and evaluation in the image segmentation tasks, not for patient-specific FEA simulation of human body deformation, we made an assumption about the strain energy density function to reduce computation cost: tissue mechanical behavior follows the Ogden hyperelastic model with homogeneous tissue properties [76,77]. The whole procedure is implemented by using our newly developed PyTorch-FEA library for large deformation biomechanics [78].

We observed that generative models, such as GAN [79,80] and diffusion [81,82], could be used to generate synthetic images for data augmentation purposes. However, the synthetic images generated by these models typically require manual annotation to obtain ground-truth labels, which is both time-consuming and labor-intensive. Our method not only generates realistic images but also produces the corresponding ground-truth labels (i.e., shapes).

### 3.5. Loss function

For each model, we use the original loss function if it is applicable to our application. If the original loss function is not suitable (e.g., it is for binary classification only), then we use the loss function  $\mathcal{L}$  that combines a Dice loss  $\mathcal{L}_{Dice}$  and an area-weighted cross entropy loss  $\mathcal{L}_{aw\_ce}$ .

$$\mathcal{L} = 0.5\mathcal{L}_{Dice} + 0.5\mathcal{L}_{aw\_ce} \quad (12)$$

$$\mathcal{L}_{Dice} = 1 - \frac{2\sum_{i,j}(y(i,j)\hat{p}_m(i,j)) + \epsilon}{\sum_{i,j}(y(i,j) + \hat{p}_m(i,j)) + \epsilon} \quad (13)$$

$$\mathcal{L}_{aw\_ce} = -\sum_{i,j,m} w_m y_m(i,j) \log(\hat{p}_m(i,j)) \quad (14)$$

$\hat{p}_m(i,j)$  is the  $m$ -th element in the output tensor from the softmax layer at the pixel location  $(i,j)$ , which corresponds to the  $m$ -th object (a disc or a vertebra) at the location  $(i,j)$ .  $y(i,j)$  is the true label of the pixel at location  $(i,j)$ .  $w_m$  is a nonnegative weight inversely proportional to the area of the  $m$ -th object, and  $\sum_m w_m = 1$ .  $\epsilon$  is a small constant ( $1e-4$ ) to prevent the case of  $0/0$  in Eq.(13). In a lumbar spine image, where the background area is substantially larger than the combined area of the discs and vertebrae, employing area-weighted cross entropy loss effectively reduces the influence of the background in the loss function.

## 4. Experiments

### 4.1. Original Dataset and Augmented Datasets

Our dataset consists of a total of 100 patients' lumbar spine T2-weighted MR images from the University of Miami medical school, with personal identification information removed. Following the protocol in [83], five lumbar discs (D1, D2, D3, D4, D5) and six vertebral bones (L1, L2, L3, L4, L5, S1) in each patient's mid-sagittal MR image was manually annotated by three trained operators to identify and mark the boundaries and landmarks of the lumbar discs and vertebrae. To ensure accuracy and consistency, the three operators engaged in discussion to reach a consensus on the best annotation (i.e., ground-truth), for each mid-sagittal MR image. In the literature, lumbar disc D1 is also called L1/L2, similarly D2 for L2/L3, D3 for L3/L4, D4 for L4/L5, and D5 for L5/S1. The MR images are of various resolutions, and each of the images are resized to  $512 \times 512$ . Each image is also pre-processed independently by normalizing the intensities into range  $[0,1]$ . The average pixel spacing is 0.7004 mm. The dataset of 100 patients was divided into 70 training samples, 10 validation samples, and 20 test samples, and those samples are referred to as the original training/validation/test samples in this paper.

Subsequently, the augmented dataset, named SSMSpine, is generated by using our method in Section 3.4. The SSMSpine dataset not only contains realistic lumbar spine MR images but also includes the corresponding ground-truth labels. The SSMSpine dataset is divided into three sets: an augmented training set with 7000 samples, an augmented validation set with 250 samples, and an augmented test set with 2500 samples. To generate the

augmented test set, an SSM was constructed using the 20 original test samples, and then 125 virtual shapes were generated from the SSM. Using each of the 20 original test samples as a reference image and each of the 125 virtual shapes,  $20 \times 125 (=2500)$  new MR images were generated using the method in Section 3.4. The augmented training and validation sets were generated in a similar way using another SSM built on both the original training and validation samples. 70 original training samples and 100 virtual shapes were used to generate the augmented training set, consisting of 7000 samples. 10 original validation samples and 25 virtual shapes were used to generate the augmented validation set, consisting of 250 samples. More information about the SSMSpine dataset is available on GitHub.

#### 4.2. Model evaluation and comparison

In our study, we trained and compared a total of 16 models on our lumbar spine MRI dataset. These models are SymTC (ours), Attention U-Net [14], HSNet [57], Inception-SwinUnet [47], MedT [23], MultiResUNet [15], SLT-Net [45], Swin-Unet [17], UNETR [21], Swin UNETR [20], TransUNet [36], UCTransNet [24], UNet++ [13], UNeXt [16], UTNet [18], and BianqueNet [53]. Due to either unavailability (e.g., no source code) or incompatibility (e.g., size not matching), we were unable to test all models mentioned in Section 2 (**Related Work**). By training and evaluating these models, we aimed to compare their performance and determine the most effective approach for spine MRI instance segmentation on our dataset. To ensure compatibility with our dataset, we made minor adjustments to the original codes of some models if necessary.

We conducted two experiments: experiment-A and experiment-B. In experiment-A, each model is trained using the original training set with elastic deformation (Section 3.4). The top 5 models in experiment-A are selected for training using the augmented training set in experiment-B. In both experiments, we applied random translations to the input images within 16 pixels during training, which is a common data augmentation method. In both experiments, the augmented validation set is used for hyper-parameter tuning. The evaluation process is divided into two parts: instance segmentation evaluation and translation robustness evaluation.

In the instance segmentation evaluation, we assess model segmentation performance for individual lumbar spine instances/objects in the MR images. The instance segmentation task is formulated as a task of labeling 12 distinct objects (5 lumbar discs, 6 vertebrae, and 1 background). The input to each model is a single-channel mid-sagittal lumbar spine MR image with size of  $512 \times 512$  pixels. In the segmentation output, each class is represented by a distinct channel as a binary segmentation map. We employ both the Dice Similarity Coefficient (DSC) and the 95% Hausdorff Distance (HD95) as evaluation metrics. In both experiments, the original test set with 20 samples and the augmented test set with 2500 samples are used separately for model performance assessment on unseen data.

Apart from assessing the instance segmentation performance, we also assess model robustness against translation transformation to the images, i.e., translation robustness. We quantify a model’s translation robustness by evaluating its segmentation performance on the test set subjected to different translations in the vertical direction and horizontal direction. This part of the evaluation assesses how well the model can maintain its segmentation accuracy when the input image undergoes translation transformations, which helps ensure the model’s reliability in real-world scenarios: the spine may not be in the center of the image. We limit the translations up to 40 pixels because a greater shift would cause objects to cross or go out of the image frame boundary.

Each model was trained on a Nvidia A6000 GPU with 48GB VRAM. During the training process, a batch size of 6 was used for most of the models, except for training MedT, where a batch size of 2 was utilized due to its large model size. The Adam optimizer with an initial learning rate of 0.0001 was employed for model optimization. A low learning rate is generally preferred to ensure stable convergence during training. Although a low learning rate might slow down the convergence process, it helps avoid convergence failures. In our experiments, each model was trained for approximately 1000 epochs. This choice was made because after 1000 epochs, no further improvement was observed in the performance of the models. Additionally, gradient clipping is applied during

training to prevent potentially large gradients from causing instability in the learning process. We performed model selection based on the performance on the validation set.

#### 4.3. Results of Experiment-A with the original training set

In experiment-A, the 16 models were trained on the original training set with elastic deformation and random-shift, and then the models were evaluated on both the original test set and the augmented test set to measure instance segmentation accuracy and translation robustness. Figure 6 displays the performance of the top 5 models, and our SymTC performs the best.

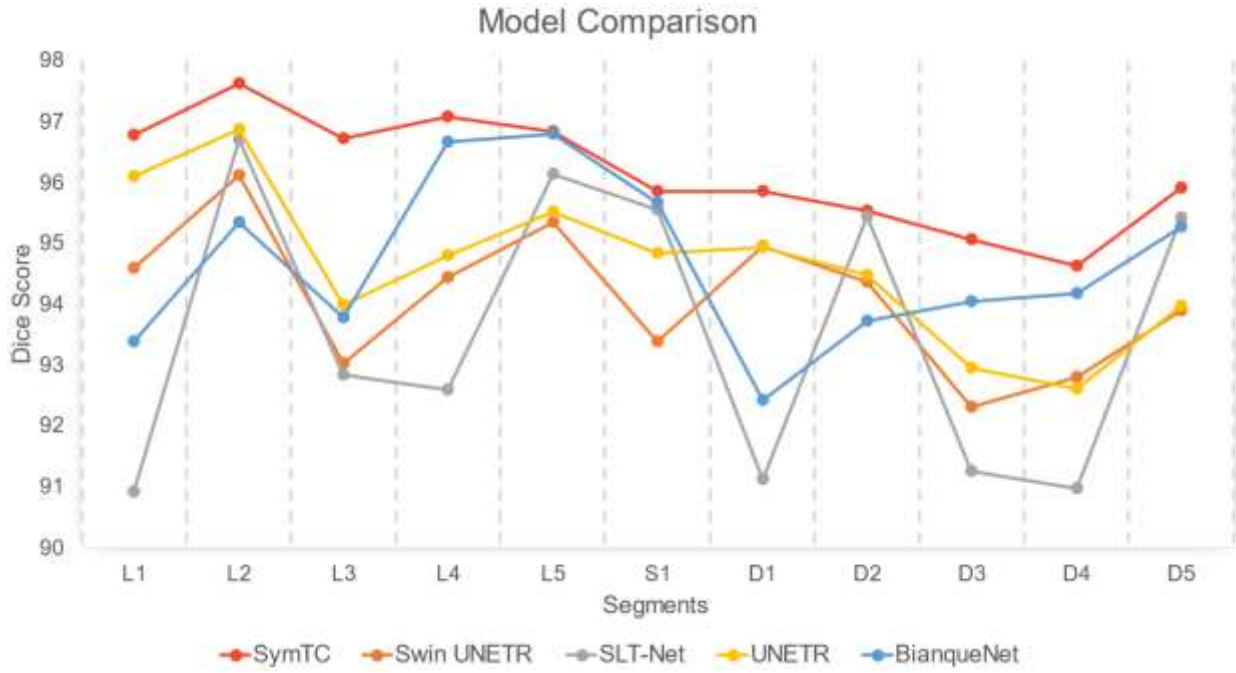


**Fig. 6.** Top 5 Model Comparison Results (DSC) on the augmented test set.

##### 4.3.1. Instance Segmentation Evaluation

Table 2 summarizes the instance segmentation results for vertebrae bodies (VB) and intervertebral discs (IVD) in terms of the DSC on the original test set consisting of 20 samples. For better clarity and ease of understanding, we have converted DSC into percentage ratios between 0 and 100%. The results show that our proposed network SymTC outperforms the other 15 models on average. SymTC stands out by achieving the highest DSC for vertebrae bodies L1, L3, L4 and intervertebral discs D1, D2, D3. SymTC along with other Transformer-based models surpasses the CNN-only models.

**Table 2.** DSC (higher is better) of each model on the original test set.

	L1	L2	L3	L4	L5	S1	D1	D2	D3	D4	D5	Average
SymTC	<b>95.598</b> ±1.791	97.010 ±1.655	<b>95.506</b> ±6.004	<b>96.531</b> ±0.959	95.319 ±4.030	93.706 ±4.263	<b>94.851</b> ±2.459	<b>94.730</b> ±4.371	<b>94.568</b> ±3.167	93.301 ±3.240	92.776 ±9.310	<b>94.900</b> ±2.095
Swin UNETR	93.126 ±7.356	96.813 ±1.641	93.874 ±11.389	95.805 ±3.189	94.380 ±4.816	92.194 ±6.449	92.757 ±4.568	94.299 ±3.519	92.821 ±6.563	89.777 ±7.645	91.077 ±10.179	93.357 ±4.098
SLT-Net	91.967 ±6.991	97.052 ±0.902	94.328 ±10.261	93.619 ±13.504	95.763 ±2.553	93.805 ±1.815	92.990 ±4.893	92.938 ±6.914	90.282 ±16.896	91.481 ±5.639	92.589 ±6.048	93.347 ±5.886
UNETR	94.355 ±3.131	96.795 ±1.709	91.900 ±18.125	95.546 ±3.196	94.099 ±3.814	92.988 ±4.539	93.261 ±3.878	93.554 ±4.254	90.931 ±9.003	90.435 ±5.678	91.446 ±4.198	93.210 ±4.333

BianqueNet	89.330 ±21.689	93.332 ±16.860	91.819 ±18.667	95.245 ±6.709	<b>96.011</b> ±2.155	<b>94.193</b> ±5.037	90.069 ±21.017	92.566 ±9.930	93.635 ±4.852	<b>93.539</b> ±3.373	<b>94.326</b> ±4.325	93.097 ±2.840
Inception-SwinUnet	91.397 ±19.415	<b>97.335</b> ±0.812	91.926 ±20.366	93.837 ±12.637	91.156 ±18.678	91.592 ±8.410	93.533 ±4.614	93.281 ±7.055	89.739 ±20.753	87.727 ±14.249	91.233 ±11.216	92.069 ±9.514
HSNet	94.240 ±12.384	94.116 ±10.544	90.123 ±22.355	91.649 ±21.243	93.456 ±11.688	92.662 ±9.901	92.948 ±7.903	88.941 ±21.43	89.008 ±21.266	89.158 ±17.099	91.986 ±12.085	91.662 ±13.085
Swin-Unet	90.839 ±20.912	93.514 ±16.261	91.781 ±21.085	91.781 ±21.08	90.076 ±21.037	92.197 ±6.612	91.638 ±11.014	90.000 ±20.632	89.755 ±20.720	87.864 ±20.629	88.554 ±16.934	90.727 ±16.984
UNeXt	92.354 ±15.512	95.835 ±4.808	91.220 ±21.036	89.282 ±21.93	88.818 ±18.828	87.325 ±14.428	92.082 ±9.072	91.271 ±16.774	87.280 ±21.834	85.790 ±19.574	89.065 ±17.579	90.029 ±18.849
TransUNet	92.245 ±9.199	87.526 ±25.59	88.178 ±24.371	91.605 ±21.122	91.219 ±21.025	89.705 ±20.496	81.444 ±32.928	86.309 ±24.176	88.812 ±21.076	88.060 ±20.596	90.294 ±20.782	88.672 ±20.293
MedT	88.707 ±20.984	94.461 ±8.57	91.011 ±20.989	90.999 ±20.981	87.121 ±25.111	87.183 ±15.317	87.639 ±20.944	89.689 ±19.384	87.318 ±20.279	82.663 ±23.855	85.180 ±22.131	88.361 ±18.641
UTNet	81.322 ±33.18	82.886 ±31.442	85.159 ±29.06	88.802 ±24.539	90.776 ±20.988	87.080 ±14.823	77.511 ±32.691	78.711 ±32.650	83.856 ±28.478	85.608 ±21.674	89.312 ±18.307	84.639 ±23.716
UCTransNet	75.346 ±31.945	78.997 ±28.28	81.862 ±26.04	80.907 ±29.371	86.107 ±22.629	86.968 ±20.202	80.058 ±25.635	80.407 ±22.833	76.787 ±30.266	81.144 ±25.322	88.063 ±19.596	81.513 ±20.303
Attention U-Net	74.333 ±35.642	74.288 ±33.164	68.732 ±36.905	76.499 ±29.188	86.964 ±22.583	85.474 ±25.111	73.700 ±37.113	68.943 ±37.476	68.092 ±35.719	80.147 ±25.685	87.694 ±21.912	76.806 ±25.335
UNet++	68.734 ±40.68	66.998 ±35.694	74.033 ±27.911	71.468 ±40.229	81.297 ±31.709	83.980 ±27.527	65.450 ±39.937	71.473 ±28.932	67.208 ±40.117	79.834 ±28.708	84.529 ±26.387	74.091 ±26.461
MultiResUNet	77.421 ±31.596	74.309 ±29.915	66.317 ±34.739	66.828 ±35.945	76.870 ±35.698	84.644 ±22.624	75.710 ±33.508	70.025 ±27.873	58.563 ±39.241	72.553 ±33.342	75.217 ±31.98	72.587 ±26.547

Table 3 shows the instance segmentation results measured by 95% Hausdorff distance (HD95) on the original test set. The results show that our proposed network SymTC outperforms the other 15 models on average, and it achieves the lowest HD95 for L1, L3, L4, D1, D2, D3, and D5.

**Table 3.** HD95 (lower is better) of each model on the original test set.

	L1	L2	L3	L4	L5	S1	D1	D2	D3	D4	D5	Average
SymTC	<b>1.93</b> ±1.829	2.006 ±3.88	1.949 ±2.183	<b>1.64</b> ±0.591	2.553 ±2.47	5.1 ±6.993	<b>1.134</b> ±0.449	<b>1.626</b> ±2.227	<b>1.491</b> ±0.711	2.118 ±1.234	<b>2.778</b> ±3.973	<b>2.211</b> ±1.187
Swin UNETR	8.594 ±12.047	11.024 ±33.718	2.992 ±3.483	3.147 ±6.521	3.759 ±5.905	9.454 ±13.059	19.057 ±41.678	1.894 ±2.472	3.466 ±5.801	3.814 ±3.828	8.128 ±12.917	6.848 ±10.137
SLT-Net	13.716 ±16.122	1.332 ±0.64	2.371 ±3.562	2.778 ±5.493	2.363 ±2.252	8.11 ±17.93	2.348 ±3.912	2.004 ±2.338	3.118 ±5.032	2.865 ±2.174	4.762 ±12.584	4.161 ±4.089
UNETR	3.744 ±6.201	1.512 ±1.261	3.679 ±7.65	2.237 ±1.722	5.927 ±6.302	<b>4.724</b> ±5.909	2.442 ±3.25	1.704 ±1.3	3.589 ±4.982	3.277 ±2.968	7.517 ±8.093	3.668 ±2.34
BianqueNet	5.056 ±10.105	7.158 ±15.206	3.624 ±7.993	3.375 ±7.988	<b>2.290</b> ±2.285	5.308 ±9.319	4.278 ±9.886	5.106 ±10.580	3.138 ±7.382	5.857 ±12.764	3.713 ±6.602	4.446 ±9.739
Inception-SwinUnet	3.378 ±7.275	<b>1.197</b> ±0.555	3.5 ±8.067	3.033 ±6.334	3.362 ±3.809	6.39 ±10.21	7.53 ±25.967	2.051 ±3.129	1.59 ±0.876	3.957 ±4.714	5.715 ±9.957	3.791 ±4.134
HSNet	3.006 ±6.714	3.634 ±8.238	4.121 ±8.874	3.94 ±9.34	5.547 ±11.36	5.196 ±10.482	2.869 ±7.442	5.378 ±11.527	4.145 ±9.551	5.966 ±11.862	5.045 ±11.035	4.441 ±7.376
Swin-Unet	2.131 ±3.459	2.226 ±4.686	1.753 ±1.591	1.971 ±2.484	2.767 ±2.596	4.732 ±7.47	2.221 ±3.907	2.937 ±6.313	1.679 ±1.159	<b>2.08</b> ±1.308	6.339 ±10.19	2.803 ±2.24
UNeXt	2.805 ±4.959	2.016 ±2.768	<b>1.933</b> ±1.542	7.259 ±19.018	13.485 ±17.479	10.8 ±15.286	5.98 ±14.131	2.536 ±4.028	5.69 ±15.364	7.292 ±13.081	11.01 ±15.926	6.437 ±8.162
TransUNet	7.727 ±15.874	8.556 ±20.98	9.261 ±19.824	3.836 ±9.163	4.372 ±9.063	7.595 ±12.805	8.968 ±22.198	8.662 ±19.145	3.876 ±9.056	5.176 ±10.127	4.15 ±9.494	6.562 ±11.646
MedT	8.665 ±14.016	2.557 ±2.564	6.168 ±11.39	2.386 ±2.751	7.056 ±10.149	10.406 ±10.254	5.684 ±10.784	7.024 ±11.272	63.762 ±83.727	5.359 ±8.133	18.524 ±33.337	12.508 ±7.994
UTNet	6.897 ±12.365	7.209 ±12.726	10.986 ±16.485	5.092 ±10.427	8.523 ±13.468	20.203 ±35.303	7.421 ±13.484	13.133 ±18.251	11.486 ±17.583	10.463 ±17.173	8.903 ±13.608	10.029 ±12.359
UCTransNet	11.554 ±13.053	21.176 ±20.644	30.833 ±45.698	12.752 ±15.773	11.034 ±15.015	9.536 ±15.319	20.424 ±32.647	23.576 ±27.95	20.578 ±22.595	14.814 ±16.837	7.444 ±13.146	16.702 ±12.286
Attention U-Net	9.394 ±12.866	13.821 ±17.43	16.946 ±18.222	21.225 ±32.217	10.944 ±15.876	7.474 ±13.279	13.878 ±18.345	15.805 ±19.732	28.632 ±35.708	10.027 ±15.161	7.124 ±13.263	14.116 ±13.022
UNet++	6.733 ±11.95	16.872 ±17.754	22.11 ±20.232	15.901 ±19.52	12.515 ±16.298	9.518 ±14.037	9.862 ±14.455	21.599 ±20.421	19.863 ±26.463	10.369 ±16.036	9.929 ±15.288	14.116 ±11.826
MultiResUNet	8.841 ±11.614	17.292 ±16.037	19.035 ±17.013	15.814 ±15.802	9.93 ±13.24	9.582 ±13.03	9.63 ±14.817	18.331 ±18.619	22.223 ±19.32	10.918 ±15.737	10.632 ±14.034	13.839 ±11.524

We also assessed the segmentation performance of all models on the augmented test set consisting of 2500 samples. Table 4 (DSC) and Table 5 (HD95) summarize the instance segmentation performance of each model

evaluated on the augmented test set. Our proposed network SymTC outperforms the other 15 models on average. SymTC has the highest average DSC for L1, L3, L4, L5, D1, D2, and D3, and attains the lowest HD95 for L1, L3, L4, D1, D2, D3, and D4.

**Table 4.** DSC (higher is better) of each model on the augmented test set.

	L1	L2	L3	L4	L5	S1	D1	D2	D3	D4	D5	Average
SymTC	<b>95.718</b> ±2.951	96.956 ±2.787	<b>95.265</b> ±7.417	<b>96.606</b> ±1.418	<b>96.153</b> ±1.89	94.448 ±3.89	<b>94.913</b> ±2.55	<b>94.827</b> ±4.502	<b>94.427</b> ±3.683	93.334 ±4.155	94.231 ±3.729	<b>95.171</b> ±2.144
Swin UNETR	93.108 ±8.399	96.337 ±3.289	93.286 ±14.544	95.270 ±5.054	94.695 ±4.905	93.072 ±5.52	93.127 ±5.447	94.191 ±4.227	91.970 ±9.192	90.438 ±6.799	91.308 ±6.215	93.346 ±4.983
SLT-Net	91.925 ±11.161	96.736 ±2.401	93.889 ±12.742	92.538 ±18.37	94.557 ±8.863	92.437 ±8.045	92.712 ±7.199	93.833 ±4.888	89.858 ±18.676	90.419 ±11.831	91.149 ±11.399	92.732 ±9.07
UNETR	93.839 ±6.152	96.260 ±3.454	91.773 ±18.475	94.984 ±5.13	94.052 ±5.003	89.817 ±10.051	93.039 ±3.998	93.865 ±4.332	90.486 ±9.81	90.317 ±5.791	89.976 ±6.801	92.583 ±5.384
BianqueNet	92.103 ±16.133	95.329 ±10.126	94.670 ±10.097	95.486 ±7.397	96.003 ±2.653	95.191 ±2.992	92.275 ±13.814	93.724 ±7.138	93.752 ±6.614	<b>93.384</b> ±5.339	94.187 ±4.917	94.191 ±8.996
Inception-SwinUnet	91.988 ±18.095	<b>96.977</b> ±3.847	91.923 ±20.632	92.382 ±18.076	94.237 ±8.303	92.904 ±9.058	93.660 ±6.763	93.689 ±6.904	89.551 ±20.673	88.781 ±14.933	91.991 ±7.246	92.553 ±10.665
HSNet	94.628 ±14.373	95.868 ±10.502	92.061 ±18.001	91.512 ±21.12	95.849 ±8.781	<b>95.682</b> ±3.865	93.117 ±13.282	93.874 ±10.222	89.820 ±19.811	89.645 ±17.916	<b>94.570</b> ±4.643	93.330 ±9.196
Swin-Unet	91.328 ±18.901	93.299 ±17.946	91.703 ±21.094	91.669 ±21.131	91.198 ±18.97	91.366 ±12.268	91.283 ±14.972	90.320 ±20.105	89.189 ±20.739	87.815 ±20.844	90.297 ±13.743	90.861 ±17.347
UNeXt	91.280 ±16.796	95.036 ±8.14	91.013 ±21.094	88.953 ±23.119	91.170 ±13.263	89.812 ±12.544	91.255 ±11.141	92.186 ±12.876	87.131 ±22.224	87.645 ±15.647	90.288 ±10.6	90.525 ±13.111
TransUNet	92.319 ±16.2	93.879 ±16.636	92.586 ±17.395	94.676 ±10.604	94.741 ±7.245	94.003 ±5.979	90.806 ±18.041	91.343 ±16.735	90.749 ±16.481	91.550 ±10.169	92.894 ±6.709	92.686 ±10.357
MedT	86.861 ±23.723	92.629 ±15.296	91.421 ±19.013	89.039 ±21.809	88.147 ±20.587	84.398 ±18.84	86.124 ±22.55	89.722 ±19.247	86.538 ±20.526	83.335 ±23.549	83.075 ±21.478	87.390 ±18.852
UTNet	82.709 ±28.31	80.782 ±30.95	84.073 ±26.989	85.725 ±27.893	91.096 ±16.215	91.306 ±9.014	76.822 ±30.988	80.621 ±28.224	83.916 ±27.028	85.401 ±20.584	90.734 ±11.839	84.835 ±19.788
UCTransNet	72.343 ±34.307	76.444 ±29.91	81.393 ±24.405	79.606 ±28.661	87.287 ±18.466	92.642 ±8.999	73.083 ±32.634	81.171 ±23.118	74.872 ±29.442	79.460 ±23.231	89.673 ±13.893	80.725 ±18.567
Attention U-Net	68.915 ±36.382	69.948 ±35.755	65.592 ±34.768	75.681 ±28.502	86.721 ±22.809	93.227 ±8.204	66.819 ±38.116	63.876 ±37.865	66.104 ±32.424	75.905 ±28.8	91.537 ±11.763	74.939 ±20.816
UNet++	65.096 ±40.792	69.498 ±36.367	69.993 ±31.743	66.925 ±37.244	81.392 ±28.029	90.460 ±13.191	64.565 ±40.33	72.047 ±31.75	63.061 ±38.234	72.931 ±31.167	87.159 ±20.266	73.012 ±23.317
MultiResUNet	73.766 ±33.559	72.475 ±32.877	70.752 ±32.574	70.171 ±35.186	78.962 ±32.165	87.809 ±18.254	68.730 ±36.759	69.854 ±34.213	68.738 ±34.452	72.479 ±33.345	79.657 ±28.326	73.945 ±25.091

**Table 5.** HD95 value (lower is better) of each model on the augmented test set.

	L1	L2	L3	L4	L5	S1	D1	D2	D3	D4	D5	Average
SymTC	<b>2.188</b> ±3.968	1.984 ±3.787	<b>2.047</b> ±2.456	<b>1.741</b> ±1.435	2.234 ±2.999	4.668 ±10.907	<b>1.566</b> ±3.679	<b>1.79</b> ±3.219	<b>1.739</b> ±2.695	<b>2.204</b> ±1.461	4.064 ±9.357	<b>2.384</b> ±2.108
Swin UNETR	11.353 ±33.189	9.468 ±31.478	7.005 ±23.16	5.783 ±17.828	5.375 ±11.093	16.07 ±35.564	13.829 ±40.509	3.708 ±15.61	6.191 ±18.392	4.775 ±11.302	11.15 ±17.265	8.609 ±15.102
SLT-Net	8.464 ±17.817	2.537 ±9.812	3.463 ±9.614	3.078 ±8.708	3.766 ±9.767	5.409 ±15.909	3.96 ±15.752	2.376 ±5.825	3.835 ±13.919	4.023 ±10.257	5.751 ±11.967	4.242 ±7.772
UNETR	5.873 ±10.615	2.63 ±6.155	4.111 ±7.566	2.506 ±3.004	5.014 ±7.516	10.871 ±19.237	2.772 ±4.803	2.103 ±3.727	4.111 ±6.555	3.735 ±4.708	6.404 ±8.943	4.557 ±4.305
BianqueNet	5.555 ±10.365	5.767 ±13.823	3.398 ±8.156	3.173 ±6.849	3.318 ±7.518	3.540 ±11.313	5.303 ±11.274	5.818 ±15.604	2.231 ±4.499	2.868 ±6.468	3.384 ±7.982	4.032 ±10.045
Inception-SwinUnet	3.41 ±10.003	<b>1.529</b> ±5.754	3.685 ±10.956	3.125 ±7.22	4.276 ±10.702	5.534 ±13.91	1.677 ±3.326	2.424 ±7.185	3.671 ±9.82	3.923 ±6.581	6.093 ±11.203	3.577 ±5.158
HSNet	2.575 ±6.116	2.72 ±9.091	3.826 ±9.386	2.955 ±7.523	<b>1.958</b> ±5.101	<b>2.37</b> ±4.584	2.165 ±6.245	2.778 ±7.9	3.13 ±8.164	2.894 ±6.34	<b>2.258</b> ±6.682	2.693 ±4.533
Swin-Unet	3.718 ±12.477	2.281 ±9.182	2.092 ±5.183	2.044 ±5.193	4.841 ±11.639	5.539 ±9.335	2.601 ±10.854	2.392 ±9.554	2.351 ±4.736	2.735 ±5.601	6.01 ±10.775	3.305 ±4.993
UNeXt	7.212 ±18.727	4.233 ±12.846	4.913 ±16.54	7.77 ±17.801	11.646 ±17.788	9.462 ±21.051	8.457 ±20.29	3.848 ±10.381	7.327 ±19.721	7.806 ±12.668	11.651 ±16.133	7.666 ±9.932
TransUNet	6.245 ±18.622	6.008 ±18.599	6.191 ±17.579	5.246 ±18.663	6.385 ±20.503	7.016 ±19.462	5.417 ±18.977	6.688 ±23.985	7.87 ±21.105	5.241 ±14.506	9.589 ±24.032	6.718 ±13.318
MedT	8.115 ±12.876	3.878 ±6.953	4.385 ±7.671	5.283 ±9.288	10.009 ±13.817	13.935 ±16.408	6.139 ±11.146	4.428 ±9.506	72.075 ±82.33	8.635 ±16.218	12.997 ±17.864	13.625 ±9.645
UTNet	8.667 ±17.117	10.592 ±20.449	15.484 ±20.453	9.202 ±17.838	14.237 ±27.825	14.724 ±22.491	10.674 ±16.985	15.102 ±21.452	11.572 ±19.287	10.649 ±18.77	8.581 ±16.592	11.771± 11.935
UCTransNet	14.267 ±20.828	21.247 ±25.68	23.542 ±31.268	20.769 ±31.321	12.504 ±16.412	9.226 ±22.252	21.576 ±32.676	27.888 ±31.415	28.971 ±34.852	17.921 ±25.073	10.608 ±19.215	18.956 ±13.438

Attention U-Net	21.033 ±29.85	18.984 ±20.704	22.082 ±22.065	31.271 ±36.969	11.244 ±20.511	6.783 ±16.671	18.986 ±25.984	19 ±21.259	32.27 ±31.194	19.275 ±26.051	11.469 ±28.816	19.309 ±14.67
UNet++	18.011 ±27.449	16.192 ±19.325	23.953 ±20.546	18.749 ±21.889	12.423 ±16.826	6.939 ±12.271	13.378 ±20.277	20.232 ±21.096	25.36 ±30.082	17.679 ±20.881	8.728 ±15.29	16.513 ±12.019
MultiResUNet	13.291 ±19.988	16.623 ±17.923	20.534 ±20.18	16.424 ±18.717	8.357 ±12.915	7.503 ±11.828	13.491 ±20.581	20.504 ±23.767	19.608 ±22.555	11.27 ±16.494	8.239 ±13.843	14.168 ±11.371

To further compare the performance, we conducted a Paired t-Test (parametric) and a Kolmogorov-Smirnov test (non-parametric) using the results on the augmented test set with 2500 samples. The null hypothesis is that the paired segmentation performance between SymTC and another model is the same. Given that the p-values of both the parametric and non-parametric statistical tests are less than 0.05, we reject the null hypothesis and conclude that the paired instance segmentation performance between SymTC and each of the other 15 methods is significantly different. We conducted the statistical tests on the augmented test set because conventional inferential statistics may lack validity for small sample sizes ( $n < 30$ ), and larger sample sizes may be necessary in heavy-tailed distributions [84–86].

The results in Tables 2-5 highlight the superior performance and effectiveness of SymTC in consistently achieving top instance segmentation results across both DSC and HD95 evaluation criteria on both the original and augmented test sets. It is also evident that Transformer-based models surpass traditional CNN-only models in instance segmentation performance.

Figure 7 shows segmentation examples of the 16 models. It is evident that SymTC accurately identifies all vertebrae and lumbar discs in the lumbar MR image, whereas other models produce misclassifications or fragmentation errors. For example, BianqueNet exhibits hollow holes in both D3 and D4. TransUNet incorrectly identifies D3 as D2 and exhibits a significant segmentation error in the lower left corner in the MR scan. Because DSC and HD95 capture distinct aspects of segmentation performance, it is important to take both into account. Even though SymTC may have a slightly lower DSC compared to BianqueNet in Figure 7, SymTC achieves a significantly lower HD95 than BianqueNet. As a result, the segmentation results depicted in Figure 7 appear to be more realistic and accurate when using SymTC, highlighting the importance of considering both DSC and HD95 for a comprehensive evaluation. Also seen in Figure 7, many other models produce incorrect predictions around pixels in close proximity to the boundary of two adjacent objects, and SymTC demonstrates superior boundary delineation. Due to our method’s consideration of pixel-wise dependencies encoded with the proposed relative position embedding, it demonstrates a more effective learning of these dependencies compared to other methods. This results in our predictions being more accurate, as there are less misclassified pixels near object boundaries.

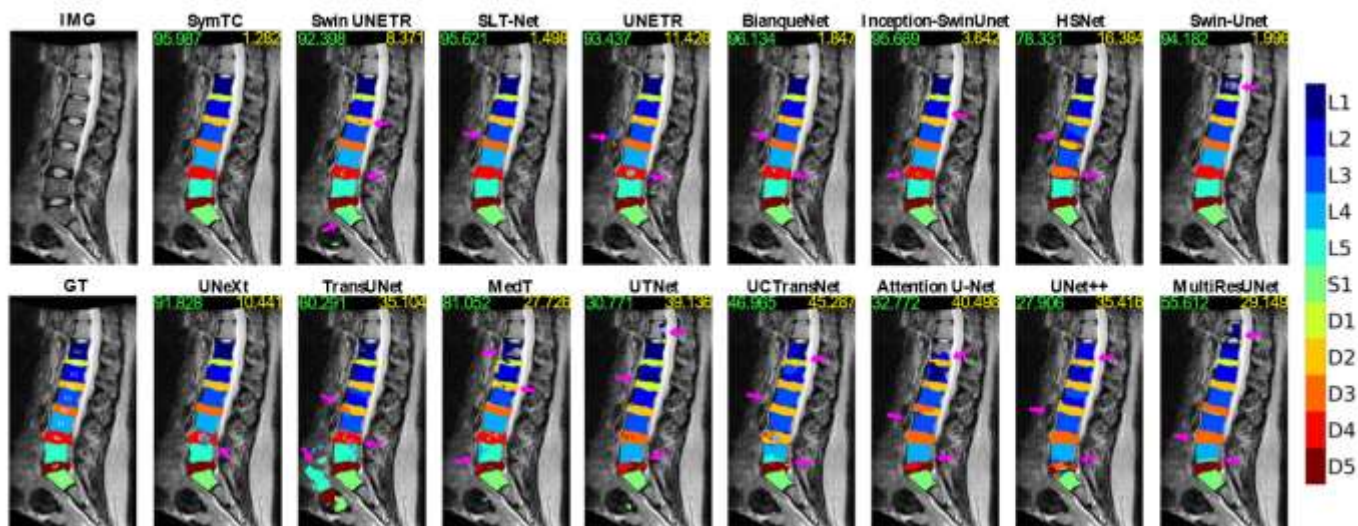


**Fig. 7.** Segmentation examples of the 16 models. IMG is the input image. GT indicates the Ground-Truth annotation. DSC (green color) and HD95 (yellow color) are shown on top corners of each image. The 11 lumbar objects are shown in different colors. Large segmentation errors are indicated by pink arrows.

#### 4.3.2. Translation Robustness Evaluation

We also assess the translation robustness of our SymTC model in comparison to other models. Our objective is to assess the performance of an instance segmentation model when it encounters shifted MR images. This assessment provides insights into a model’s ability to generalize and maintain reliability in the real scenario where the overall position of the spine on an image may vary.

Table 6 and Table 7 exhibit each model’s resilience in response to image shifts in the horizontal direction and the vertical direction, respectively. SymTC has the highest robustness performance in the horizontal direction, and it also has the highest robustness performance when the vertical translation is constrained within 20 pixels. BianqueNet excels in the case of vertical translation ranging from 20 to 40 pixels. We note the robustness of SymTC will increase when training on the large augmented training set in experiment-B (see Section 4.4.2).

**Table 6.** DSC results (higher is better) of horizontal-shift robustness experiment on the augmented test set. The displacement values are 10, 20, 30, 40 (pixels). An image could be shifted to the left or to the right. The results of left-shift and right-shift with the same displacement are averaged.

	0	10	20	30	40
SymTC	<b>95.171</b> ±2.144	<b>95.159</b> ±2.181	<b>95.110</b> ±2.293	<b>95.010</b> ±2.472	<b>94.789</b> ±2.848
Swin UNETR	93.346 ±4.983	93.297 ±5.113	93.123 ±5.545	92.745 ±6.252	92.098 ±7.266
SLT-Net	92.732 ±9.070	92.752 ±8.977	92.626 ±9.404	92.346 ±10.338	92.067 ±11.260
UNETR	92.583 ±5.384	92.390 ±5.708	91.764 ±6.634	89.973 ±8.216	85.782 ±10.576
BianqueNet	94.191 ±5.633	94.181 ±5.660	94.158 ±5.706	94.158 ±5.684	94.137 ±5.669
Inception-SwinUnet	92.553 ±10.665	92.447 ±11.029	92.176 ±11.950	91.827 ±12.897	91.389 ±13.927
HSNet	93.330 ±9.196	93.366 ±8.990	93.407 ±8.908	93.347 ±9.076	93.333 ±8.993
Swin-Unet	90.861 ±17.347	90.717 ±17.550	90.353 ±17.975	89.849 ±18.228	88.785 ±18.755
UneXt	90.525 ±13.111	90.466 ±13.164	90.450 ±13.175	90.484 ±13.166	90.415 ±13.239
TransUNet	92.686 ±10.357	92.679 ±10.362	92.700 ±10.191	92.721 ±10.089	92.782 ±9.797
MedT	87.390 ±18.852	87.295 ±18.962	87.011 ±19.186	86.485 ±19.497	85.693 ±19.878
UTNet	84.835 ±19.788	84.786 ±19.748	84.292 ±19.990	83.662 ±20.260	83.643 ±20.269
UCTransNet	80.725 ±18.567	80.648 ±18.658	80.381 ±18.740	79.983 ±18.880	79.339 ±19.091

Attention U-Net	74.939 ±20.816	74.857 ±20.886	74.892 ±20.875	74.893 ±20.883	74.880 ±20.850
Unet++	73.012 ±23.317	72.886 ±23.393	72.934 ±23.352	72.972 ±23.349	72.892 ±23.347
MultiResUNet	73.945 ±25.091	73.935 ±25.078	73.892 ±25.150	73.958 ±25.086	73.962 ±25.086

**Table 7.** DSC results (higher is better) of vertical-shift robustness experiment on the augmented test set. The displacement values are 10, 20, 30, 40 (pixels). An image could be shifted up or down. The results of up-shift and down-shift with the same displacement are averaged.

	0	10	20	30	40
SymTC	<b>95.171</b> ±2.144	<b>95.075</b> ±2.918	<b>94.299</b> ±6.097	88.772 ±15.911	65.746 ±28.109
Swin UNETR	93.346 ±4.983	93.349 ±5.195	91.459 ±9.470	74.140 ±23.991	40.481 ±21.560
SLT-Net	92.732 ±9.070	92.545 ±9.744	91.022 ±11.802	70.455 ±25.555	38.540 ±17.218
UNETR	92.583 ±5.384	92.349 ±5.903	90.150 ±10.968	73.600 ±26.210	29.801 ±23.044
BianqueNet	94.191 ±5.633	94.557 ±4.733	94.297 ±5.533	<b>93.050</b> ±8.311	<b>89.889</b> ±12.777
Inception-SwinUnet	92.553 ±10.665	92.535 ±10.533	91.177 ±12.514	80.521 ±21.338	54.437 ±24.638
HSNet	93.330 ±9.196	93.741 ±8.389	93.538 ±9.012	92.465 ±10.983	89.213 ±15.011
Swin-Unet	90.861 ±17.347	90.636 ±17.501	89.176 ±18.612	73.142 ±26.973	38.689 ±21.415
UneXt	90.525 ±13.111	90.632 ±13.205	89.622 ±14.364	85.245 ±17.722	75.723 ±21.031
TransUNet	92.686 ±10.357	92.802 ±10.377	92.416 ±10.624	90.996 ±11.931	85.995 ±15.036
MedT	87.390 ±18.852	87.375 ±18.907	84.770 ±19.918	76.460 ±24.128	59.687 ±27.708
UTNet	84.835 ±19.788	84.781 ±19.880	83.949 ±20.203	82.269 ±20.667	79.665 ±21.264
UCTransNet	80.725 ±18.567	80.316 ±18.875	78.338 ±19.653	75.076 ±20.717	71.053 ±21.402
Attention U-Net	74.939 ±20.816	74.997 ±20.791	75.251 ±20.859	75.328 ±20.816	75.199 ±20.960
Unet++	73.012 ±23.317	73.030 ±23.300	73.091 ±23.300	73.190 ±23.302	72.890 ±23.295
MultiResUNet	73.945 ±25.091	74.170 ±25.118	74.513 ±25.140	74.424 ±25.160	74.223 ±25.127

While the CNN-only models do not attain high DSC for instance segmentation, these models exhibit a notable degree of stability and consistency in the translation robustness experiments. This is attributed to the translation invariance property inherent to CNNs, which makes these models less susceptible to translations in the images. Conversely, Transformer-based models necessitate processing global information, which can pose challenges in dealing with positional shifts. Unlike CNN-only models, which benefit from their translation

invariance property, Transformer-based models depend on capturing contextual relationships and dependencies among various elements within the input data. Consequently, the introduction of positional shifts in the input can disrupt the position information in Transformers, leading to potential impacts on the segmentation output. This underscores the limitation of Transformer-based models in the context of instance segmentation tasks and emphasizes the necessity to effectively preserve the relative position information in the input images.

We also observe that, when comparing vertical robustness experiments to horizontal robustness experiments, all models exhibit subpar performance. The models are more sensitive to shifts in the vertical direction than in the horizontal direction. This is due to the inherent property of spine MRI scans, wherein the texture and structure along the vertical direction provide more informative features than those along the horizontal direction.

#### 4.4. Results of Experiment-B with the augmented training set

In this section, we show the advantages of our data augmentation method in Section 3.4. The top five models in Table 2 are SymTC, Swin UNETR, SLT-Net, UNETR, and BianqueNet. In the experiment-B, each of the five models was trained from scratch using the augmented training set consisting of 7000 samples. Model evaluations were conducted on both the original test set (see Table 8 and Table 9) and the augmented test set (see Table 10 and Table 11). The results show that the segmentation performances of most models are improved, suggesting that the augmented data can enhance the generalization and overall performance of a model. SymTC exhibits the highest average instance segmentation performance compared to the other four models.

It is noteworthy that training Transformer-based models with limited data is challenging. Nevertheless, the new data augmentation method effectively tackles the challenge of data scarcity with the support of SSM and biomechanics. Our data augmentation can generate synthetic images that closely resemble real data, effectively enhancing the model training process. This approach assists in augmenting the available data, enabling Transformer models to learn from a more diverse and representative dataset. The augmented/synthesized datasets can be made publicly available without any concerns related to medical data privacy.

By using the instance segmentation evaluation and the additional translation robustness assessment, a comprehensive evaluation of each model’s performance is achieved. This ensures that models excel not only in instance segmentation ability but also maintain their accuracy under realistic and varied conditions.

##### 4.4.1. Instance Segmentation Evaluation

Table 8 (DSC) and Table 9 (HD95) present the instance segmentation evaluations of the five models on the original test set. It is important to note that the three models have shown improvement in both DSC and HD95. This indicates that our augmented training dataset has indeed enhanced the generalization and performance of the models on previously unseen data. SymTC, in particular, continues to exhibit the best average instance segmentation performance.

**Table 8.** DSC results (higher is better) of each model on the original test set. The “change” is the DSC difference when training on the augmented training set as opposed to training on the original training set.

Network	L1	L2	L3	L4	L5	S1	D1	D2	D3	D4	D5	Average	Change
SymTC	<b>96.816</b> ±0.751	<b>97.418</b> ±0.793	<b>96.350</b> ±3.726	<b>97.025</b> ±0.911	<b>96.728</b> ±1.917	94.089 ±5.211	<b>95.449</b> ±2.457	95.004 ±3.991	<b>94.747</b> ±3.819	<b>93.640</b> ±3.778	<b>95.398</b> ±1.742	<b>95.697</b> ±3.253	<b>+0.797</b>
Swin UNETR	95.557 ±2.545	97.156 ±1.916	94.463 ±10.808	95.426 ±6.947	94.238 ±8.987	91.819 ±8.224	94.585 ±3.476	93.744 ±5.749	93.511 ±7.831	89.653 ±13.524	91.254 ±10.718	93.764 ±8.387	<b>+2.687</b>
SLT-Net	91.590 ±21.053	96.189 ±5.735	92.721 ±18.353	89.381 ±23.918	91.403 ±21.091	90.406 ±20.637	90.319 ±20.655	<b>95.059</b> ±3.031	92.061 ±12.894	85.353 ±24.918	90.444 ±20.790	91.357 ±19.053	<b>-1.990</b>

UNETR	95.874 ±2.757	96.896 ±1.548	93.962 ±11.395	95.139 ±7.462	95.622 ±2.924	<b>94.609</b> ±2.357	94.566 ±2.761	94.035 ±4.634	93.233 ±7.606	91.491 ±6.922	93.619 ±4.509	94.458 ±5.924	<b>+1.248</b>
BianqueNet	87.489 ±27.764	89.546 ±24.220	90.307 ±19.149	93.448 ±11.174	94.369 ±6.939	93.031 ±6.960	85.923 ±28.719	88.646 ±9.390	91.167 ±11.079	87.369 ±17.608	91.668 ±11.856	90.269 ±18.575	<b>-2.828</b>

**Table 9.** HD95 results (lower is better) of each model on the original test set. The “change” is the HD95 difference when training on the augmented training set as opposed to training on the original training set.

Network	L1	L2	L3	L4	L5	S1	D1	D2	D3	D4	D5	Average	Change
SymTC	<b>1.280</b> ±0.489	1.933 ±3.834	<b>1.784</b> ±2.279	<b>1.449</b> ±0.812	<b>1.721</b> ±1.719	5.426 ±11.004	<b>1.057</b> ±0.417	1.558 ±2.270	<b>1.429</b> ±0.916	<b>2.043</b> ±1.488	3.462 ±6.542	<b>2.104</b> ±4.392	<b>-0.107</b>
Swin UNETR	25.542 ±51.669	4.810 ±16.491	10.771 ±40.426	9.623 ±35.968	2.767 ±3.436	17.774 ±37.188	7.049 ±21.414	9.973 ±35.002	1.481 ±1.111	2.975 ±3.206	11.992 ±16.526	9.524 ±29.767	<b>+2.676</b>
SLT-Net	3.727 ±7.864	<b>1.627</b> ±2.401	3.233 ±7.368	2.239 ±4.187	4.125 ±8.733	<b>4.014</b> ±7.567	1.936 ±3.702	<b>1.461</b> ±1.533	3.101 ±7.624	5.300 ±10.626	4.700 ±10.386	3.224 ±7.289	<b>-0.937</b>
UNETR	2.333 ±3.715	1.715 ±2.224	2.753 ±4.274	2.525 ±4.489	2.623 ±2.789	4.075 ±6.766	1.380 ±0.580	1.922 ±2.882	2.279 ±3.703	2.551 ±2.389	<b>2.256</b> ±1.511	2.401 ±3.641	<b>-1.267</b>
BianqueNet	4.809 ±10.395	4.665 ±10.792	7.094 ±16.348	3.756 ±8.038	5.245 ±10.295	9.090 ±15.080	4.773 ±11.239	6.979 ±16.887	8.547 ±23.035	5.799 ±11.210	7.777 ±13.558	6.230 ±14.053	<b>+1.784</b>

Table 10 (DSC) and Table 11 (HD95) present the instance segmentation evaluation results on the augmented test set. It is evident that the segmentation performances of all models have improved by using the augmented training dataset, as indicated by enhancements in both evaluation metrics, except for Swin UNETR on the HD95 metric. The augmented training dataset offers a broader domain, enabling the models to acquire more diverse knowledge and achieve improved segmentation performance. This increased resilience to data variations is a notable benefit of the augmented training dataset. Increasing the complexity of the training dataset helps prevent overfitting and regulating models from memorizing the training. Furthermore, SymTC maintains the best average instance segmentation performance on both evaluation metrics.

**Table 10.** DSC results (higher is better) of each model on the augmented test set. The “change” is the DSC difference when training on the augmented training set as opposed to training on the original training set.

	L1	L2	L3	L4	L5	S1	D1	D2	D3	D4	D5	Average	Change
SymTC	<b>96.767</b> ±1.020	<b>97.618</b> ±0.766	<b>96.723</b> ±2.621	<b>97.081</b> ±1.120	<b>96.825</b> ±1.389	<b>95.855</b> ±1.912	<b>95.862</b> ±1.873	<b>95.541</b> ±3.147	<b>95.054</b> ±3.446	<b>94.624</b> ±2.479	<b>95.912</b> ±1.390	<b>96.169</b> ±2.277	<b>+0.998</b>
Swin UNETR	94.593 ±8.113	96.124 ±7.352	93.027 ±17.824	94.442 ±12.723	95.345 ±6.840	93.384 ±6.406	94.949 ±3.461	94.369 ±7.674	92.323 ±13.660	92.806 ±5.711	93.900 ±4.372	94.115 ±9.581	<b>+0.769</b>
SLT-Net	90.928 ±21.398	96.708 ±5.097	92.836 ±18.462	92.604 ±19.937	96.143 ±4.279	95.545 ±2.669	91.135 ±18.062	95.435 ±3.448	91.254 ±17.130	90.982 ±15.676	95.427 ±2.972	93.545 ±14.102	<b>+0.813</b>
UNETR	96.099 ±2.574	96.878 ±2.479	93.981 ±11.711	94.798 ±8.922	95.509 ±3.888	94.832 ±2.951	94.930 ±2.159	94.486 ±5.341	92.957 ±8.036	92.616 ±4.935	93.974 ±3.926	94.642 ±6.081	<b>+2.059</b>
BianqueNet	93.381 ±16.166	95.339 ±12.916	93.786 ±13.760	96.670 ±4.308	96.789 ±2.243	95.666 ±2.302	92.427 ±16.211	93.723 ±11.633	94.040 ±7.633	94.184 ±4.318	95.276 ±3.268	94.662 ±10.231	<b>+0.471</b>

**Table 11.** HD95 results (lower is better) of each model on the augmented test set. The “change” is the HD95 difference when training on the augmented training set as opposed to training on the original training set.

	L1	L2	L3	L4	L5	S1	D1	D2	D3	D4	D5	Average	Change
SymTC	<b>1.268</b> ±0.597	<b>1.185</b> ±1.971	<b>1.824</b> ±2.371	<b>1.375</b> ±0.741	<b>1.603</b> ±1.612	<b>1.803</b> ±2.546	<b>1.057</b> ±1.692	1.517 ±2.297	<b>1.475</b> ±1.776	<b>1.799</b> ±1.189	<b>1.559</b> ±3.059	<b>1.497</b> ±1.959	<b>-0.887</b>
Swin UNETR	17.591 ±52.428	13.865 ±44.911	12.207 ±42.917	11.290 ±38.870	10.393 ±35.903	19.144 ±52.802	9.570 ±35.018	12.249 ±43.617	7.145 ±30.825	5.524 ±21.039	11.808 ±30.508	11.889 ±40.236	<b>+3.280</b>
SLT-Net	3.720 ±8.774	1.577 ±3.310	3.227 ±7.838	1.899 ±5.205	2.012 ±2.264	1.871 ±2.843	2.344 ±6.312	<b>1.387</b> ±2.514	3.100 ±8.190	2.584 ±4.752	1.602 ±2.714	2.302 ±5.549	<b>-1.940</b>
UNETR	1.923 ±2.598	1.774 ±3.164	2.679 ±4.416	3.029 ±7.859	3.056 ±5.502	3.340 ±5.462	1.329 ±1.5817	1.788 ±2.9369	2.348 ±3.860	2.640 ±3.108	2.455 ±3.079	2.396 ±4.341	<b>-2.161</b>
BianqueNet	3.815 ±9.985	2.907 ±8.092	3.849 ±10.217	2.605 ±9.389	2.268 ±7.335	2.667 ±10.589	3.383 ±9.089	4.257 ±11.508	3.149 ±10.065	2.061 ±5.126	2.860 ±13.087	3.075 ±9.734	<b>-0.957</b>

We conducted both Paired t-Test (parametric) and Kolmogorov-Smirnov Test (non-parametric) statistical analyses between SymTC and each of the other four methods. The p-values obtained from both statistical tests are less than 0.05, indicating that the average segmentation performance of SymTC is significantly different/better from that of the other models.

#### 4.4.2. Translation Robustness Evaluation

Table 12 (horizontal-shift) and Table 13 (vertical-shift) present the translation robustness results of the five models on the augmented test set consisting of 2500 samples. As depicted in Table 12, the horizontal robustness of all models has improved. Additionally, Table 13 indicates that vertical-robustness performances have also improved. This demonstrates that our data augmentation method effectively supplements the feature space, being beneficial for enhancing model robustness.

It is important to note that a vertical translation larger than 30 pixels could cause the top or bottom vertebra to cross image boundary, and such a scenario may introduce confusion for the models, as they could miss essential information for precise segmentation.

**Table 12.** DSC results (higher is better) of horizontal-shit robustness experiment of the five models. The displacement values are 10, 20, 30, 40 (pixels). An image could be shifted to the left and to the right. The results of left-shift and right-shift with the same displacement are averaged.

	0	10	20	30	40
SymTC	<b>96.169</b> ±1.146	<b>96.169</b> ±1.152	<b>96.168</b> ±1.157	<b>96.167</b> ±1.165	<b>96.165</b> ±1.173
Swin UNETR	94.115 ±7.661	94.088 ±7.744	94.014 ±8.018	93.904 ±8.429	93.725 ±9.049
SLT-Net	93.545 ±8.636	93.493 ±8.643	93.376 ±8.822	93.355 ±9.031	93.308 ±9.128
UNETR	94.642 ±4.260	94.639 ±4.300	94.617 ±4.439	94.461 ±5.404	94.052 ±7.824
BianqueNet	94.662 ±7.024	94.628 ±7.144	94.640 ±7.096	94.627 ±7.108	94.626 ±7.155

**Table 13.** DSC results (higher is better) of vertical-shit robustness experiment of the five models. The displacement values are 10, 20, 30, 40 (pixels). An image could be shifted up or down. The results of up-shift and down-shift with the same displacement are averaged.

	0	10	20	30	40
SymTC	<b>96.169</b> ±1.146	<b>96.169</b> ±1.156	<b>96.138</b> ±1.310	<b>95.389</b> ±4.481	85.737 ±13.248
Swin UNETR	94.115 ±7.661	94.045 ±8.019	93.361 ±10.034	83.586 ±20.367	43.519 ±16.969
SLT-Net	93.545 ±8.636	93.235 ±9.180	92.334 ±10.872	86.659 ±17.703	68.053 ±22.927
UNETR	94.642 ±4.260	94.637 ±4.235	94.447 ±5.148	92.124 ±12.617	59.598 ±32.013
BianqueNet	94.662 ±7.024	95.165 ±5.578	95.299 ±5.161	94.430 ±7.430	<b>92.777</b> ±10.775

#### 4.5. Ablation Study

In this section, we perform various ablation experiments to investigate the significance and contribution of different configurations of hyperparameters, such as Transformer layers, attention heads, and embedding dimension, within our proposed model. These ablation experiments allow us to assess the effectiveness of our model in enforcing global structural regularity during the training phase, offering insights into the impact of different hyperparameter choices. In Tables 14-17, the bold settings indicate the default configuration in our SymTC. These variations of SymTC are trained on the original training set and tested on the augmented test set.

Table 14 presents the results of ablation study assessing the impact of Transformer path and CNN path within each SymTC module. The term ‘‘CNN only’’ refers to a configuration where all Transformer layers are turned off, and ‘‘Transformer only’’ indicates that all CNN layers are disabled. The results reveal that the configuration of the best instance segmentation performance is achieved by deactivating the Transformer path in TCM-2. It also reveals that the Transformer path is more crucial in the TC module when comparing the instance segmentation performance of ‘‘CNN only’’ and ‘‘Transformer only’’ configurations. This underlines the significant contribution of the Transformer path in enhancing the instance segmentation capabilities of SymTC. However, it is noted that the ‘‘CNN only’’ configuration exhibits superior translation robustness. Furthermore, turning off the CNN path in SymTC modules closer to the input would have a more negative impact on segmentation performance than doing so in modules near the output. There is no definitive evidence pointing to a specific TC module as being the most significant for improving either segmentation performance or translation robustness.

**Table 14.** DSC results (higher is better) of ablation study by switching on/off Transformer layers in SymTC. The other settings are unchanged. TCM-n represents the TC module #n in SymTC.

SymTC Settings	Horizontal Translation				Vertical Translation		
	0	10	20	40	10	20	40
<b>CNN + Transformer</b>	95.171	95.159	95.110	<b>94.789</b>	95.075	94.299	65.746
CNN only	81.366	81.564	81.477	81.551	82.000	81.946	<b>81.530</b>
Transformer only	93.166	93.146	93.066	92.389	93.098	92.059	45.748
Disable Transformer in TCM-0	95.157	95.136	95.076	94.588	95.068	94.424	67.213
Disable Transformer in TCM-1	95.086	95.082	95.008	94.689	95.063	93.841	48.990
Disable Transformer in TCM-2	<b>95.234</b>	<b>95.212</b>	95.152	94.742	<b>95.207</b>	94.221	53.556
Disable Transformer in TCM-3	95.040	95.026	94.948	94.409	95.041	93.762	49.539
Disable CNN in TCM-0	94.093	94.098	94.069	93.883	94.036	93.4513	62.493

Disable CNN in TCM-1	94.441	94.415	94.359	93.964	94.472	93.722	32.271
Disable CNN in TCM-2	94.939	94.939	94.918	94.678	94.969	93.069	34.890
Disable CNN in TCM-3	95.217	95.203	<b>95.158</b>	94.757	95.197	<b>94.563</b>	60.887

Table 15 summarizes the results obtained by varying the number of Transformer layers in SymTC modules for comparison purposes. The results show that the impact of the number of Transformer layers on instance segmentation performance is very minimal, indicating a few Transformer layers are good enough because a larger number of Transformer layers leads to higher computation cost. For translation robustness, it is evident that increasing the number of Transformer layers in each SymTC module leads to improved robustness in general.

**Table 15.** DSC results (higher is better) of ablation study by varying the number of Transformer layers in a TCM of SymTC. The other settings are unchanged.

Num. of layers in a TCM	Horizontal Translation				Vertical Translation		
	0	10	20	40	10	20	40
2	95.171	95.159	95.110	94.789	95.075	94.299	65.746
4	95.224	95.215	95.162	94.650	95.235	94.864	52.375
6	95.177	95.170	95.137	94.811	95.193	<b>94.922</b>	52.657
8	<b>95.387</b>	<b>95.389</b>	95.370	95.221	<b>95.390</b>	94.916	43.878
10	95.158	95.160	95.141	94.953	95.198	94.700	58.711
12	95.204	95.247	95.196	94.917	95.215	94.439	64.501
14	95.380	95.378	95.367	95.251	95.371	94.410	38.823
16	95.383	95.386	<b>95.375</b>	<b>95.297</b>	95.377	94.233	61.896
18	95.304	95.289	95.269	95.038	95.296	94.821	<b>70.426</b>

Table 16 presents the impact of head counts in the Multi-Head Self-Attention (MHSA) component of the SymTC modules. SymTC modules with a larger number of heads exhibit increased immunity to image shifting in the horizontal direction. The number of heads does not have much impact on the segmentation performance with zero-translation.

**Table 16.** DSC results (higher is better) of ablation study by varying the number of heads in Transformer layers of SymTC. The other settings are unchanged.

Num. of heads	Horizontal Translation				Vertical Translation		
	0	10	20	40	10	20	40
4	95.069	95.056	95.018	94.749	95.060	94.408	41.276
8	95.146	95.122	95.052	94.718	95.101	94.337	53.339
<b>16</b>	95.171	95.159	95.110	94.700	95.075	94.299	65.746
32	95.026	94.997	94.919	94.481	94.992	94.257	63.183
64	<b>95.196</b>	<b>95.174</b>	95.149	94.907	<b>95.146</b>	94.553	<b>69.629</b>
128	94.999	94.959	94.878	94.413	95.041	94.125	66.479

256	95.122	95.104	<b>95.151</b>	<b>94.984</b>	95.127	<b>94.708</b>	40.093
-----	--------	--------	---------------	---------------	--------	---------------	--------

Table 17 shows the influence of the embedding dimension in Transformers within the SymTC modules. It demonstrates enhancement in segmentation performance and horizontal robustness with the increase in the embedding dimension. However, when the embedding dimension reaches 1024, there is a small drop in both segmentation performance and horizontal robustness, which suggests that increasing the embedding dimension beyond a certain threshold may lead to diminishing returns and negatively impact.

**Table 17.** DSC results (higher is better) of ablation study by varying the embedding dimension in Transformer layers of SymTC. The other settings are unchanged.

Embedding Dimension	Horizontal Translation				Vertical Translation		
	0	10	20	40	10	20	40
32	93.779	93.713	93.595	92.788	94.011	92.633	<b>71.897</b>
64	94.260	94.220	94.085	93.267	94.345	93.071	64.206
128	94.743	94.708	94.572	93.915	94.683	93.306	53.252
256	94.588	94.568	94.482	93.952	94.468	93.370	59.848
<b>512</b>	<b>95.171</b>	<b>95.159</b>	<b>95.110</b>	<b>94.789</b>	95.075	94.299	65.746
1024	95.104	95.080	95.007	94.625	<b>95.091</b>	<b>94.429</b>	57.398

## 5. Conclusion

In this paper, we present SymTC together with SSM-biomechanics based data augmentation, a dedicated approach to address the challenge of achieving precise instance segmentation of lumbar spine MR images. The performance of SymTC has been demonstrated through the comprehensive experiments and comparison with the other 15 existing models using our datasets, including the original dataset of 100 patients, and the generated SSMSpine dataset of thousands of virtual patients.

SymTC introduces a symbiotic relationship between CNN and Transformer that runs in two parallel paths in each TC module, which excels in assimilating both local and global contextual information from the spine MR images. This dual-path approach enables SymTC to achieve much better segmentation accuracy, compared to the models only using CNN or Transformer layers. The SymTC architecture also incorporates a novel relative position embedding that is specifically designed to fuse spatial information between content and position effectively, capturing and integrating critical spatial information. This relative position embedding elevates the model’s capability in image segmentation.

We developed the SSM-biomechanics based data augmentation method to further improve model performance by providing large and diverse datasets of synthetic images with ground-truth labels. Given that our augmented datasets consist entirely of synthetic data, we have made our augmented dataset (SSMSpine) publicly available. The results presented indicate that models trained on the augmented training set had comparably or even better performance than the same models trained on the original training set. This underscores that our data augmentation method can generate synthetic data that eliminates privacy concerns while retaining in the same image domain.

Our current study mainly focused on the mid-sagittal lumbar spine MR images for two major reasons. First, as shown in a clinical study [83], the mid-sagittal image of a patient provides the most useful information for the diagnosis of lumbar spine degeneration. Secondly, the slice thickness of a lumbar MR scan in the sagittal direction is often much larger than 5mm, which causes difficulties to create accurate 3D ground-truth annotation for model training. Nevertheless, our model could be directly extended to handle 3D images once the sagittal slice thickness becomes acceptably small with the advancement of imaging technology.

### CrediT authorship contribution statement

**Jiasong Chen:** Data curation, Conceptualization, Formal analysis, Investigation, Methodology, Software, Validation, Visualization, Writing – original draft. **Linchen Qian:** Data curation, Investigation, Software, Writing – review & editing. **Linhai Ma:** Investigation, Writing – review & editing. **Timur Urakov:** Data curation, Writing – review & editing. **Weiyong Gu:** Writing – review & editing. **Liang Liang:** Methodology, Supervision, Project administration, Resources, Writing – review.

### Declaration of competing interest

The authors declare that they have no known competing financial interests or personal relationships that could have appeared to influence the work reported in this paper.

### References

- [1] M. Cox, R. Serra, I. Shapiro, M. Risbud, *The Intervertebral Disc: Molecular and Structural Studies of the Disc in Health and Disease*, (2014).
- [2] N. Kos, L. Gradisnik, T. Velnar, A Brief Review of the Degenerative Intervertebral Disc Disease, *Med. Arch.* 73 (2019) 421–424. <https://doi.org/10.5455/medarh.2019.73.421-424>.
- [3] C.A. Mallio, G. Vadalà, F. Russo, C. Bernetti, L. Ambrosio, B.B. Zobel, C.C. Quattrocchi, R. Papalia, V. Denaro, Novel Magnetic Resonance Imaging Tools for the Diagnosis of Degenerative Disc Disease: A Narrative Review, *Diagnostics* 12 (2022) 420. <https://doi.org/10.3390/diagnostics12020420>.
- [4] S. Roberts, C. Gardner, Z. Jiang, A. Abedi, Z. Buser, J.C. Wang, Analysis of trends in lumbar disc degeneration using kinematic MRI, *Clin. Imaging* 79 (2021) 136–141. <https://doi.org/10.1016/j.clinimag.2021.04.028>.
- [5] S. Tamagawa, D. Sakai, H. Nojiri, M. Sato, M. Ishijima, M. Watanabe, Imaging Evaluation of Intervertebral Disc Degeneration and Painful Discs—Advances and Challenges in Quantitative MRI, *Diagnostics* 12 (2022) 707. <https://doi.org/10.3390/diagnostics12030707>.
- [6] F. Galbusera, G. Casaroli, T. Bassani, Artificial intelligence and machine learning in spine research, *JOR SPINE* 2 (2019) e1044. <https://doi.org/10.1002/jsp2.1044>.
- [7] C. Chevretils, F. Chériet, G. Grimard, C.-E. Aubin, Watershed Segmentation of Intervertebral Disk and Spinal Canal from MRI Images, in: M. Kamel, A. Campilho (Eds.), *Image Anal. Recognit.*, Springer, Berlin, Heidelberg, 2007: pp. 1017–1027. [https://doi.org/10.1007/978-3-540-74260-9\\_90](https://doi.org/10.1007/978-3-540-74260-9_90).
- [8] Y.L. Huang, D.R. Chen, Watershed segmentation for breast tumor in 2-D sonography. *Ultrasound Med. Biol.* 30, 2004: pp. 625–632. <https://doi.org/10.1016/j.ultrasmedbio.2003.12.001>
- [9] J. Huang, F. Jian, H. Wu, H. Li, An improved level set method for vertebra CT image segmentation, *Biomed. Eng. OnLine* 12 (2013) 48. <https://doi.org/10.1186/1475-925X-12-48>.
- [10] N. Li, M. Liu, Y. Li, Image Segmentation Algorithm using Watershed Transform and Level Set Method, in: 2007 IEEE Int. Conf. Acoust. Speech Signal Process. - ICASSP 07, 2007: p. I-613-I-616. <https://doi.org/10.1109/ICASSP.2007.365982>.

- [11] S. Suganyadevi, V. Seethalakshmi, K. Balasamy, A review on deep learning in medical image analysis, *Int. J. Multimed. Inf. Retr.* 11 (2022) 19–38. <https://doi.org/10.1007/s13735-021-00218-1>.
- [12] D. Shen, G. Wu, H.-I. Suk, Deep Learning in Medical Image Analysis, *Annu. Rev. Biomed. Eng.* 19 (2017) 221–248. <https://doi.org/10.1146/annurev-bioeng-071516-044442>.
- [13] Z. Zhou, M.M. Rahman Siddiquee, N. Tajbakhsh, J. Liang, UNet++: A Nested U-Net Architecture for Medical Image Segmentation, in: D. Stoyanov, Z. Taylor, G. Carneiro, T. Syeda-Mahmood, A. Martel, L. Maier-Hein, J.M.R.S. Tavares, A. Bradley, J.P. Papa, V. Belagiannis, J.C. Nascimento, Z. Lu, S. Conjeti, M. Moradi, H. Greenspan, A. Madabhushi (Eds.), *Deep Learn. Med. Image Anal. Multimodal Learn. Clin. Decis. Support*, Springer International Publishing, Cham, 2018: pp. 3–11. [https://doi.org/10.1007/978-3-030-00889-5\\_1](https://doi.org/10.1007/978-3-030-00889-5_1).
- [14] O. Oktay, J. Schlemper, L.L. Folgoc, M. Lee, M. Heinrich, K. Misawa, K. Mori, S. McDonagh, N.Y. Hammerla, B. Kainz, B. Glocker, D. Rueckert, Attention U-Net: Learning Where to Look for the Pancreas, (2018). <https://doi.org/10.48550/arXiv.1804.03999>.
- [15] N. Ibtehaz, M.S. Rahman, MultiResUNet : Rethinking the U-Net architecture for multimodal biomedical image segmentation, *Neural Netw.* 121 (2020) 74–87. <https://doi.org/10.1016/j.neunet.2019.08.025>.
- [16] J.M.J. Valanarasu, V.M. Patel, UNeXt: MLP-Based Rapid Medical Image Segmentation Network, in: L. Wang, Q. Dou, P.T. Fletcher, S. Speidel, S. Li (Eds.), *Med. Image Comput. Comput. Assist. Interv. – MICCAI 2022*, Springer Nature Switzerland, Cham, 2022: pp. 23–33. [https://doi.org/10.1007/978-3-031-16443-9\\_3](https://doi.org/10.1007/978-3-031-16443-9_3).
- [17] H. Cao, Y. Wang, J. Chen, D. Jiang, X. Zhang, Q. Tian, M. Wang, Swin-Unet: Unet-Like Pure Transformer for Medical Image Segmentation, in: L. Karlinsky, T. Michaeli, K. Nishino (Eds.), *Comput. Vis. – ECCV 2022 Workshop*, Springer Nature Switzerland, Cham, 2023: pp. 205–218. [https://doi.org/10.1007/978-3-031-25066-8\\_9](https://doi.org/10.1007/978-3-031-25066-8_9).
- [18] Y. Gao, M. Zhou, D.N. Metaxas, UTNet: A Hybrid Transformer Architecture for Medical Image Segmentation, in: M. de Bruijne, P.C. Cattin, S. Cotin, N. Padoy, S. Speidel, Y. Zheng, C. Essert (Eds.), *Med. Image Comput. Comput. Assist. Interv. – MICCAI 2021*, Springer International Publishing, Cham, 2021: pp. 61–71. [https://doi.org/10.1007/978-3-030-87199-4\\_6](https://doi.org/10.1007/978-3-030-87199-4_6).
- [19] Y. Huang, X. Yang, L. Liu, H. Zhou, A. Chang, X. Zhou, R. Chen, J. Yu, J. Chen, C. Chen, S. Liu, H. Chi, X. Hu, K. Yue, L. Li, V. Grau, D.-P. Fan, F. Dong, D. Ni, Segment anything model for medical images?, *Med. Image Anal.* 92 (2024) 103061. <https://doi.org/10.1016/j.media.2023.103061>.
- [20] A. Hatamizadeh, V. Nath, Y. Tang, D. Yang, H.R. Roth, D. Xu, Swin UNETR: Swin Transformers for Semantic Segmentation of Brain Tumors in MRI Images, in: A. Crimi, S. Bakas (Eds.), *Brainlesion Glioma Mult. Scler. Stroke Trauma. Brain Inj.*, Springer International Publishing, Cham, 2022: pp. 272–284. [https://doi.org/10.1007/978-3-031-08999-2\\_22](https://doi.org/10.1007/978-3-031-08999-2_22).
- [21] A. Hatamizadeh, Y. Tang, V. Nath, D. Yang, A. Myronenko, B. Landman, H. Roth, D. Xu, UNETR: Transformers for 3D Medical Image Segmentation, (2021). <https://doi.org/10.48550/arXiv.2103.10504>.
- [22] Y. Hu, L. Zhang, N. Mu, L. Liu, Parameter-Efficient Transformer with Hybrid Axial-Attention for Medical Image Segmentation, (2022). <https://doi.org/10.48550/arXiv.2211.09533>.
- [23] J.M.J. Valanarasu, P. Oza, I. Hacihaliloglu, V.M. Patel, Medical Transformer: Gated Axial-Attention for Medical Image Segmentation, in: M. de Bruijne, P.C. Cattin, S. Cotin, N. Padoy, S. Speidel, Y. Zheng, C. Essert (Eds.), *Med. Image Comput. Comput. Assist. Interv. – MICCAI 2021*, Springer International Publishing, Cham, 2021: pp. 36–46. [https://doi.org/10.1007/978-3-030-87193-2\\_4](https://doi.org/10.1007/978-3-030-87193-2_4).
- [24] H. Wang, P. Cao, J. Wang, O.R. Zaiane, UCTransNet: Rethinking the Skip Connections in U-Net from a Channel-Wise Perspective with Transformer, *Proc. AAAI Conf. Artif. Intell.* 36 (2022) 2441–2449. <https://doi.org/10.1609/aaai.v36i3.20144>.
- [25] A. Sekuboyina, J. Kukačka, J.S. Kirschke, B.H. Menze, A. Valentinitzsch, Attention-Driven Deep Learning for Pathological Spine Segmentation, in: B. Glocker, J. Yao, T. Vrtovec, A. Frangi, G. Zheng (Eds.), *Comput. Methods Clin. Appl. Musculoskelet. Imaging*, Springer International Publishing, Cham, 2018: pp. 108–119. [https://doi.org/10.1007/978-3-319-74113-0\\_10](https://doi.org/10.1007/978-3-319-74113-0_10).

- [26] B. Wang, J. Qin, L. Lv, M. Cheng, L. Li, D. Xia, S. Wang, MLKCA-Unet: Multiscale large-kernel convolution and attention in Unet for spine MRI segmentation, *Optik* 272 (2023) 170277. <https://doi.org/10.1016/j.ijleo.2022.170277>.
- [27] S. Moccia, E. De Momi, S. El Hadji, L.S. Mattos, Blood vessel segmentation algorithms — Review of methods, datasets and evaluation metrics, *Comput. Methods Programs Biomed.* 158 (2018) 71–91. <https://doi.org/10.1016/j.cmpb.2018.02.001>.
- [28] T.A. Soomro, A.J. Afifi, L. Zheng, S. Soomro, J. Gao, O. Hellwich, M. Paul, Deep Learning Models for Retinal Blood Vessels Segmentation: A Review, *IEEE Access* 7 (2019) 71696–71717. <https://doi.org/10.1109/ACCESS.2019.2920616>.
- [29] H. Berhane, M. Scott, M. Elbaz, K. Jarvis, P. McCarthy, J. Carr, C. Malaisrie, R. Avery, A.J. Barker, J.D. Robinson, C.K. Rigsby, M. Markl, Fully automated 3D aortic segmentation of 4D flow MRI for hemodynamic analysis using deep learning, *Magn. Reson. Med.* 84 (2020) 2204–2218. <https://doi.org/10.1002/mrm.28257>.
- [30] J.M.H. Noothout, B.D. de Vos, J.M. Wolterink, I. Išgum, Automatic segmentation of thoracic aorta segments in low-dose chest CT, in: *Med. Imaging 2018 Image Process.*, SPIE, 2018: pp. 446–451. <https://doi.org/10.1117/12.2293114>.
- [31] A. Pepe, J. Li, M. Rolf-Pissarczyk, C. Gsaxner, X. Chen, G.A. Holzapfel, J. Egger, Detection, segmentation, simulation and visualization of aortic dissections: A review, *Med. Image Anal.* 65 (2020) 101773. <https://doi.org/10.1016/j.media.2020.101773>.
- [32] A. Vaswani, N. Shazeer, N. Parmar, J. Uszkoreit, L. Jones, A.N. Gomez, Ł. Kaiser, I. Polosukhin, Attention is All you Need, in: *Adv. Neural Inf. Process. Syst.*, Curran Associates, Inc., 2017. [https://proceedings.neurips.cc/paper\\_files/paper/2017/hash/3f5ee243547dee91fbd053c1c4a845aa-Abstract.html](https://proceedings.neurips.cc/paper_files/paper/2017/hash/3f5ee243547dee91fbd053c1c4a845aa-Abstract.html) (accessed August 22, 2023).
- [33] F. Shamshad, S. Khan, S.W. Zamir, M.H. Khan, M. Hayat, F.S. Khan, H. Fu, Transformers in medical imaging: A survey, *Med. Image Anal.* 88 (2023) 102802. <https://doi.org/10.1016/j.media.2023.102802>.
- [34] Y. Zhao, X. Chen, B. McDonald, C. Yu, A.S.R. Mohamed, C.D. Fuller, L.E. Court, T. Pan, H. Wang, X. Wang, J. Phan, J. Yang, A transformer-based hierarchical registration framework for multimodality deformable image registration, *Comput. Med. Imaging Graph.* 108 (2023) 102286. <https://doi.org/10.1016/j.compmedimag.2023.102286>.
- [35] G.Q. Hong, Y.T. Wei, W.A.W. Morley, M. Wan, A.J. Mertens, Y. Su, H.-L.M. Cheng, Dual-domain accelerated MRI reconstruction using transformers with learning-based undersampling, *Comput. Med. Imaging Graph.* 106 (2023) 102206. <https://doi.org/10.1016/j.compmedimag.2023.102206>.
- [36] J. Chen, Y. Lu, Q. Yu, X. Luo, E. Adeli, Y. Wang, L. Lu, A.L. Yuille, Y. Zhou, TransUNet: Transformers Make Strong Encoders for Medical Image Segmentation, (2021). <https://doi.org/10.48550/arXiv.2102.04306>.
- [37] Z. Liu, Y. Lin, Y. Cao, H. Hu, Y. Wei, Z. Zhang, S. Lin, B. Guo, Swin Transformer: Hierarchical Vision Transformer using Shifted Windows, (2021). <https://doi.org/10.48550/arXiv.2103.14030>.
- [38] B. Xie, G. Milam, B. Ning, J. Cha, C.H. Park, DXM-TransFuse U-net: Dual cross-modal transformer fusion U-net for automated nerve identification, *Comput. Med. Imaging Graph.* 99 (2022) 102090. <https://doi.org/10.1016/j.compmedimag.2022.102090>.
- [39] H. Jiang, M. Imran, P. Muralidharan, A. Patel, J. Pensa, M. Liang, T. Benidir, J.R. Grajo, J.P. Joseph, R. Terry, J.M. DiBianco, L.-M. Su, Y. Zhou, W.G. Brisbane, W. Shao, MicroSegNet: A deep learning approach for prostate segmentation on micro-ultrasound images, *Comput. Med. Imaging Graph.* 112 (2024) 102326. <https://doi.org/10.1016/j.compmedimag.2024.102326>.
- [40] X. Li, S. Pang, R. Zhang, J. Zhu, X. Fu, Y. Tian, J. Gao, ATTransUNet: An enhanced hybrid transformer architecture for ultrasound and histopathology image segmentation, *Comput. Biol. Med.* 152 (2023) 106365. <https://doi.org/10.1016/j.compbiomed.2022.106365>.
- [41] Q. He, Q. Yang, M. Xie, HCTNet: A hybrid CNN-transformer network for breast ultrasound image segmentation, *Comput. Biol. Med.* 155 (2023) 106629. <https://doi.org/10.1016/j.compbiomed.2023.106629>.

- [42] Z. Ma, Y. Qi, C. Xu, W. Zhao, M. Lou, Y. Wang, Y. Ma, ATFE-Net: Axial Transformer and Feature Enhancement-based CNN for ultrasound breast mass segmentation, *Comput. Biol. Med.* 153 (2023) 106533. <https://doi.org/10.1016/j.compbimed.2022.106533>.
- [43] K. Sirinukunwattana, J.P.W. Pluim, H. Chen, X. Qi, P.-A. Heng, Y.B. Guo, L.Y. Wang, B.J. Matuszewski, E. Bruni, U. Sanchez, A. Böhm, O. Ronneberger, B.B. Cheikh, D. Racoceanu, P. Kainz, M. Pfeiffer, M. Urschler, D.R.J. Snead, N.M. Rajpoot, Gland segmentation in colon histology images: The glas challenge contest, *Med. Image Anal.* 35 (2017) 489–502. <https://doi.org/10.1016/j.media.2016.08.008>.
- [44] B. Landman, Z. Xu, J. Igelsias, M. Styner, T. Langerak, A. Klein, Miccai multi-atlas labeling beyond the cranial vault—workshop and challenge, in: 2015: p. 12. <https://doi.org/10.7303/syn3193805>.
- [45] K. Feng, L. Ren, G. Wang, H. Wang, Y. Li, SLT-Net: A codec network for skin lesion segmentation, *Comput. Biol. Med.* 148 (2022) 105942. <https://doi.org/10.1016/j.compbimed.2022.105942>.
- [46] X. Dong, J. Bao, D. Chen, W. Zhang, N. Yu, L. Yuan, D. Chen, B. Guo, CSWin Transformer: A General Vision Transformer Backbone with Cross-Shaped Windows, (2022). <https://doi.org/10.48550/arXiv.2107.00652>.
- [47] Y. Pu, Q. Zhang, C. Qian, Q. Zeng, N. Li, L. Zhang, S. Zhou, G. Zhao, Semi-supervised segmentation of coronary DSA using mixed networks and multi-strategies, *Comput. Biol. Med.* 156 (2023) 106493. <https://doi.org/10.1016/j.compbimed.2022.106493>.
- [48] P. Dufter, M. Schmitt, H. Schütze, Position Information in Transformers: An Overview, *Comput. Linguist.* 48 (2022) 733–763. [https://doi.org/10.1162/coli\\_a\\_00445](https://doi.org/10.1162/coli_a_00445).
- [49] P. Shaw, J. Uszkoreit, A. Vaswani, Self-Attention with Relative Position Representations, (2018). <https://doi.org/10.48550/arXiv.1803.02155>.
- [50] X. Kuang, J.P. Cheung, H. Wu, S. Dokos, T. Zhang, MRI-SegFlow: a novel unsupervised deep learning pipeline enabling accurate vertebral segmentation of MRI images, in: 2020 42nd Annu. Int. Conf. IEEE Eng. Med. Biol. Soc. EMBC, 2020: pp. 1633–1636. <https://doi.org/10.1109/EMBC44109.2020.9175987>.
- [51] S. Pang, C. Pang, Z. Su, L. Lin, L. Zhao, Y. Chen, Y. Zhou, H. Lu, Q. Feng, DGMSNet: Spine segmentation for MR image by a detection-guided mixed-supervised segmentation network, *Med. Image Anal.* 75 (2022) 102261. <https://doi.org/10.1016/j.media.2021.102261>.
- [52] L.-C. Chen, Y. Zhu, G. Papandreou, F. Schroff, H. Adam, Encoder-Decoder with Atrous Separable Convolution for Semantic Image Segmentation, in: V. Ferrari, M. Hebert, C. Sminchisescu, Y. Weiss (Eds.), *Comput. Vis. – ECCV 2018*, Springer International Publishing, Cham, 2018: pp. 833–851. [https://doi.org/10.1007/978-3-030-01234-2\\_49](https://doi.org/10.1007/978-3-030-01234-2_49).
- [53] H.-D. Zheng, Y.-L. Sun, D.-W. Kong, M.-C. Yin, J. Chen, Y.-P. Lin, X.-F. Ma, H.-S. Wang, G.-J. Yuan, M. Yao, X.-J. Cui, Y.-Z. Tian, Y.-J. Wang, Deep learning-based high-accuracy quantitation for lumbar intervertebral disc degeneration from MRI, *Nat. Commun.* 13 (2022) 841. <https://doi.org/10.1038/s41467-022-28387-5>.
- [54] A. Dosovitskiy, L. Beyer, A. Kolesnikov, D. Weissenborn, X. Zhai, T. Unterthiner, M. Dehghani, M. Minderer, G. Heigold, S. Gelly, J. Uszkoreit, N. Houlsby, An Image is Worth 16x16 Words: Transformers for Image Recognition at Scale, (2021). <https://doi.org/10.48550/arXiv.2010.11929>.
- [55] G. Litjens, T. Kooi, B.E. Bejnordi, A.A.A. Setio, F. Ciompi, M. Ghafoorian, J.A.W.M. van der Laak, B. van Ginneken, C.I. Sánchez, A survey on deep learning in medical image analysis, *Med. Image Anal.* 42 (2017) 60–88. <https://doi.org/10.1016/j.media.2017.07.005>.
- [56] W. Wang, E. Xie, X. Li, D.-P. Fan, K. Song, D. Liang, T. Lu, P. Luo, L. Shao, PVT v2: Improved Baselines with Pyramid Vision Transformer, *Comput. Vis. Media* 8 (2022) 415–424. <https://doi.org/10.1007/s41095-022-0274-8>.
- [57] W. Zhang, C. Fu, Y. Zheng, F. Zhang, Y. Zhao, C.-W. Sham, HSNet: A hybrid semantic network for polyp segmentation, *Comput. Biol. Med.* 150 (2022) 106173. <https://doi.org/10.1016/j.compbimed.2022.106173>.
- [58] X. You, Y. Gu, Y. Liu, S. Lu, X. Tang, J. Yang, EG-Trans3DUNet: A Single-Stage Transformer-Based Model for Accurate Vertebrae Segmentation from Spinal Ct Images, in: 2022 IEEE 19th Int. Symp. Biomed. Imaging ISBI, 2022: pp. 1–5. <https://doi.org/10.1109/ISBI52829.2022.9761551>.

- [59] R. Tao, W. Liu, G. Zheng, Spine-transformers: Vertebra labeling and segmentation in arbitrary field-of-view spine CTs via 3D transformers, *Med. Image Anal.* 75 (2022) 102258. <https://doi.org/10.1016/j.media.2021.102258>.
- [60] L. Zhang, J. Yang, D. Liu, F. Zhang, S. Nie, Y. Tan, T. Guo, Spine X-ray Image Segmentation Based on Transformer and Adaptive Optimized Postprocessing, in: 2022 IEEE 2nd Int. Conf. Softw. Eng. Artif. Intell. SEAI, 2022: pp. 88–92. <https://doi.org/10.1109/SEAI55746.2022.9832144>.
- [61] S. Kirnaz, C. Capadona, T. Wong, J.L. Goldberg, B. Medary, F. Sommer, L.B. McGrath, R. Härtl, Fundamentals of Intervertebral Disc Degeneration, *World Neurosurg.* 157 (2022) 264–273. <https://doi.org/10.1016/j.wneu.2021.09.066>.
- [62] T. Lin, Y. Wang, X. Liu, X. Qiu, A survey of transformers, *AI Open* 3 (2022) 111–132. <https://doi.org/10.1016/j.aiopen.2022.10.001>.
- [63] K. Wu, H. Peng, M. Chen, J. Fu, H. Chao, Rethinking and Improving Relative Position Encoding for Vision Transformer, in: 2021 IEEE CVF Int. Conf. Comput. Vis. ICCV, IEEE, Montreal, QC, Canada, 2021: pp. 10013–10021. <https://doi.org/10.1109/ICCV48922.2021.00988>.
- [64] Z. Huang, D. Liang, P. Xu, B. Xiang, Improve Transformer Models with Better Relative Position Embeddings, (2020). <https://doi.org/10.48550/arXiv.2009.13658>.
- [65] H. Wang, Y. Zhu, B. Green, H. Adam, A. Yuille, L.-C. Chen, Axial-DeepLab: Stand-Alone Axial-Attention for Panoptic Segmentation, in: A. Vedaldi, H. Bischof, T. Brox, J.-M. Frahm (Eds.), *Comput. Vis. – ECCV 2020*, Springer International Publishing, Cham, 2020: pp. 108–126. [https://doi.org/10.1007/978-3-030-58548-8\\_7](https://doi.org/10.1007/978-3-030-58548-8_7).
- [66] Z. Zhang, W. Zhang, Pyramid Medical Transformer for Medical Image Segmentation, (2022). <https://doi.org/10.48550/arXiv.2104.14702>.
- [67] O. Ronneberger, P. Fischer, T. Brox, U-Net: Convolutional Networks for Biomedical Image Segmentation, in: N. Navab, J. Hornegger, W.M. Wells, A.F. Frangi (Eds.), *Med. Image Comput. Comput.-Assist. Interv. – MICCAI 2015*, Springer International Publishing, Cham, 2015: pp. 234–241. [https://doi.org/10.1007/978-3-319-24574-4\\_28](https://doi.org/10.1007/978-3-319-24574-4_28).
- [68] F. Ambellan, H. Lamecker, C. von Tycowicz, S. Zachow, Statistical Shape Models: Understanding and Mastering Variation in Anatomy, in: P.M. Rea (Ed.), *Biomed. Vis. Vol. 3*, Springer International Publishing, Cham, 2019: pp. 67–84. [https://doi.org/10.1007/978-3-030-19385-0\\_5](https://doi.org/10.1007/978-3-030-19385-0_5).
- [69] N. Sarkalkan, H. Weinans, A.A. Zadpoor, Statistical shape and appearance models of bones, *Bone* 60 (2014) 129–140. <https://doi.org/10.1016/j.bone.2013.12.006>.
- [70] H. Hufnagel, X. Pennec, J. Ehrhardt, H. Handels, N. Ayache, Shape Analysis Using a Point-Based Statistical Shape Model Built on Correspondence Probabilities, in: N. Ayache, S. Ourselin, A. Maeder (Eds.), *Med. Image Comput. Comput.-Assist. Interv. – MICCAI 2007*, Springer, Berlin, Heidelberg, 2007: pp. 959–967. [https://doi.org/10.1007/978-3-540-75757-3\\_116](https://doi.org/10.1007/978-3-540-75757-3_116).
- [71] R.H. Davies, C.J. Twining, P. Daniel Allen, T.F. Cootes, C.J. Taylor, Building optimal 2D statistical shape models, *Image Vis. Comput.* 21 (2003) 1171–1182. <https://doi.org/10.1016/j.imavis.2003.09.003>.
- [72] T.F. Cootes, C.J. Taylor, D.H. Cooper, J. Graham, Active Shape Models-Their Training and Application, *Comput. Vis. Image Underst.* 61 (1995) 38–59. <https://doi.org/10.1006/cviu.1995.1004>.
- [73] L. Liang, M. Liu, C. Martin, J.A. Elefteriades, W. Sun, A machine learning approach to investigate the relationship between shape features and numerically predicted risk of ascending aortic aneurysm, *Biomech. Model. Mechanobiol.* 16 (2017) 1519–1533. <https://doi.org/10.1007/s10237-017-0903-9>.
- [74] W.A. van Veldhuizen, R.C.L. Schuurmann, F.F.A. IJpma, R.H.J. Kropman, G.A. Antoniou, J.M. Wolterink, J.-P.P.M. de Vries, A Statistical Shape Model of the Morphological Variation of the Infrarenal Abdominal Aortic Aneurysm Neck, *J. Clin. Med.* 11 (2022) 1687. <https://doi.org/10.3390/jcm11061687>.
- [75] H. Wiputra, S. Matsumoto, J.E. Wagenseil, A.C. Braverman, R.K. Voeller, V.H. Barocas, Statistical shape representation of the thoracic aorta: accounting for major branches of the aortic arch, *Comput. Methods Biomech. Biomed. Engin.* 26 (2023) 1557–1571. <https://doi.org/10.1080/10255842.2022.2128672>.
- [76] R.W. Ogden, R. Hill, Large deformation isotropic elasticity – on the correlation of theory and experiment for incompressible rubberlike solids, *Proc. R. Soc. Lond. Math. Phys. Sci.* 326 (1997) 565–584. <https://doi.org/10.1098/rspa.1972.0026>.

- [77] K.Kr. Dwivedi, P. Lakhani, S. Kumar, N. Kumar, A hyperelastic model to capture the mechanical behaviour and histological aspects of the soft tissues, *J. Mech. Behav. Biomed. Mater.* 126 (2022) 105013. <https://doi.org/10.1016/j.jmbbm.2021.105013>.
- [78] L. Liang, M. Liu, J. Elefteriades, W. Sun, PyTorch-FEA: Autograd-enabled finite element analysis methods with applications for biomechanical analysis of human aorta, *Comput. Methods Programs Biomed.* 238 (2023) 107616. <https://doi.org/10.1016/j.cmpb.2023.107616>.
- [79] X. Yi, E. Walia, P. Babyn, Generative Adversarial Network in Medical Imaging: A Review, *Med. Image Anal.* 58 (2019) 101552. <https://doi.org/10.1016/j.media.2019.101552>.
- [80] C. Han, H. Hayashi, L. Rundo, R. Araki, W. Shimoda, S. Muramatsu, Y. Furukawa, G. Mauri, H. Nakayama, GAN-based synthetic brain MR image generation, in: 2018 IEEE 15th Int. Symp. Biomed. Imaging ISBI 2018, 2018: pp. 734–738. <https://doi.org/10.1109/ISBI.2018.8363678>.
- [81] F. Khader, G. Müller-Franzes, S. Tayebi Arasteh, T. Han, C. Haarbuerger, M. Schulze-Hagen, P. Schad, S. Engelhardt, B. Baeßler, S. Foersch, J. Stegmaier, C. Kuhl, S. Nebelung, J.N. Kather, D. Truhn, Denoising diffusion probabilistic models for 3D medical image generation, *Sci. Rep.* 13 (2023) 7303. <https://doi.org/10.1038/s41598-023-34341-2>.
- [82] W.H.L. Pinaya, P.-D. Tudosiu, J. Dafflon, P.F. Da Costa, V. Fernandez, P. Nachev, S. Ourselin, M.J. Cardoso, Brain Imaging Generation with Latent Diffusion Models, in: A. Mukhopadhyay, I. Oksuz, S. Engelhardt, D. Zhu, Y. Yuan (Eds.), *Deep Gener. Models*, Springer Nature Switzerland, Cham, 2022: pp. 117–126. [https://doi.org/10.1007/978-3-031-18576-2\\_12](https://doi.org/10.1007/978-3-031-18576-2_12).
- [83] X. Hu, M. Chen, J. Pan, L. Liang, Y. Wang, Is it appropriate to measure age-related lumbar disc degeneration on the mid-sagittal MR image? A quantitative image study, *Eur. Spine J.* 27 (2018) 1073–1081. <https://doi.org/10.1007/s00586-017-5357-3>.
- [84] A. Field, *Discovering statistics using IBM SPSS statistics*, sage, 2013.
- [85] E.J. Mascha, T.R. Vetter, Significance, Errors, Power, and Sample Size: The Blocking and Tackling of Statistics, *Anesth. Analg.* 126 (2018) 691–698. <https://doi.org/10.1213/ANE.0000000000002741>.
- [86] R. Wilcoxon, Chapter 5 - Comparing Two Groups, in: R. Wilcoxon (Ed.), *Introd. Robust Estim. Hypothesis Test.* Third Ed., Academic Press, Boston, 2012: pp. 137–213. <https://doi.org/10.1016/B978-0-12-386983-8.00005-6>.